

Geodynamic models of short-lived, long-lived and periodic flat slab subduction

W.P. Schellart¹ and V. Strak¹

Department of Earth Sciences, Vrije Universiteit Amsterdam, 1081 HV, Amsterdam, Netherlands. E-mail: w.p.schellart@vu.nl

Accepted 2021 March 29. Received 2021 March 22; in original form 2020 December 10

SUMMARY

Flat slab subduction has been ascribed to a variety of causes, including subduction of buoyant ridges/plateaus and forced trench retreat. The former, however, has irregular spatial correlations with flat slabs, while the latter has required external forcing in geodynamic subduction models, which might be insufficient or absent in nature. In this paper, we present buoyancy-driven numerical geodynamic models and aim to investigate flat slab subduction in the absence of external forcing as well as test the influence of overriding plate strength, subducting plate thickness, inclusion/exclusion of an oceanic plateau and lower mantle viscosity on flat slab formation and its evolution. Flat slab subduction is reproduced during normal oceanic subduction in the absence of ridge/plateau subduction and without externally forced plate motion. Subduction of a plateau-like feature, in this buoyancy-driven setting, enhances slab steepening. In models that produce flat slab subduction, it only commences after a prolonged period of slab dip angle reduction during lower mantle slab penetration. The flat slab is supported by mantle wedge suction, vertical compressive stresses at the base of the slab and upper mantle slab buckling stresses. Our models demonstrate three modes of flat slab subduction, namely short-lived (transient) flat slab subduction, long-lived flat slab subduction and periodic flat slab subduction, which occur for different model parameter combinations. Most models demonstrate slab folding at the 660 km discontinuity, which produces periodic changes in the upper mantle slab dip angle. With relatively high overriding plate strength or large subducting plate thickness, such folding results in periodic changes in the dip angle of the flat slab segment, which can lead to periodic flat slab subduction, providing a potential explanation for periodic arc migration. Flat slab subduction ends due to the local overriding plate shortening and thickening it produces, which forces mantle wedge opening and a reduction in mantle wedge suction. As overriding plate strength controls the shortening rate, it has a strong control on the duration of flat slab subduction, which increases with increasing strength. For the weakest overriding plate, flat slab subduction is short-lived and lasts only 6 Myr, while for the strongest overriding plate flat slab subduction is long-lived and exceeds 75 Myr. Progressive overriding plate shortening during flat slab subduction might explain why flat slab subduction terminated in the Eocene in western North America and in the Jurassic in South China.

Key words: Mantle processes; Numerical modelling; Continental margins: convergent; Dynamics of lithosphere and mantle; Folds and folding; Subduction zone processes.

1 INTRODUCTION

1.1 Flat slab subduction and slab dip angles

The dip angle of slabs in the Earth's mantle varies considerably, both in the shallow upper mantle and at greater depth (Jarrard 1986; Yamaoka *et al.* 1986; Gudmundsson & Sambridge 1998; Gutscher *et al.* 2000; Lallemand *et al.* 2005; Schellart 2008a; Hayes *et al.* 2012, Fig. 1). Some 69 per cent of slab segments at active subduction

zones have an average slab dip angle down to ~ 125 km depth in the range $20\text{--}40^\circ$ (normal dip angle, Fig. 1o). Those with a steep slab dip angle ($>40^\circ$) take up some 17 per cent. These slab segments, representing ~ 86 per cent of slab segments at active subduction zones on Earth, are generally characterized by one convex-upward hinge zone in the uppermost 100–200 km, which is located close to the trench (Figs 1d, e, m and n). The remaining 14 per cent consist of subduction segments with an anomalously low average slab dip angle down to ~ 125 km depth ($\leq 20^\circ$) and are generally

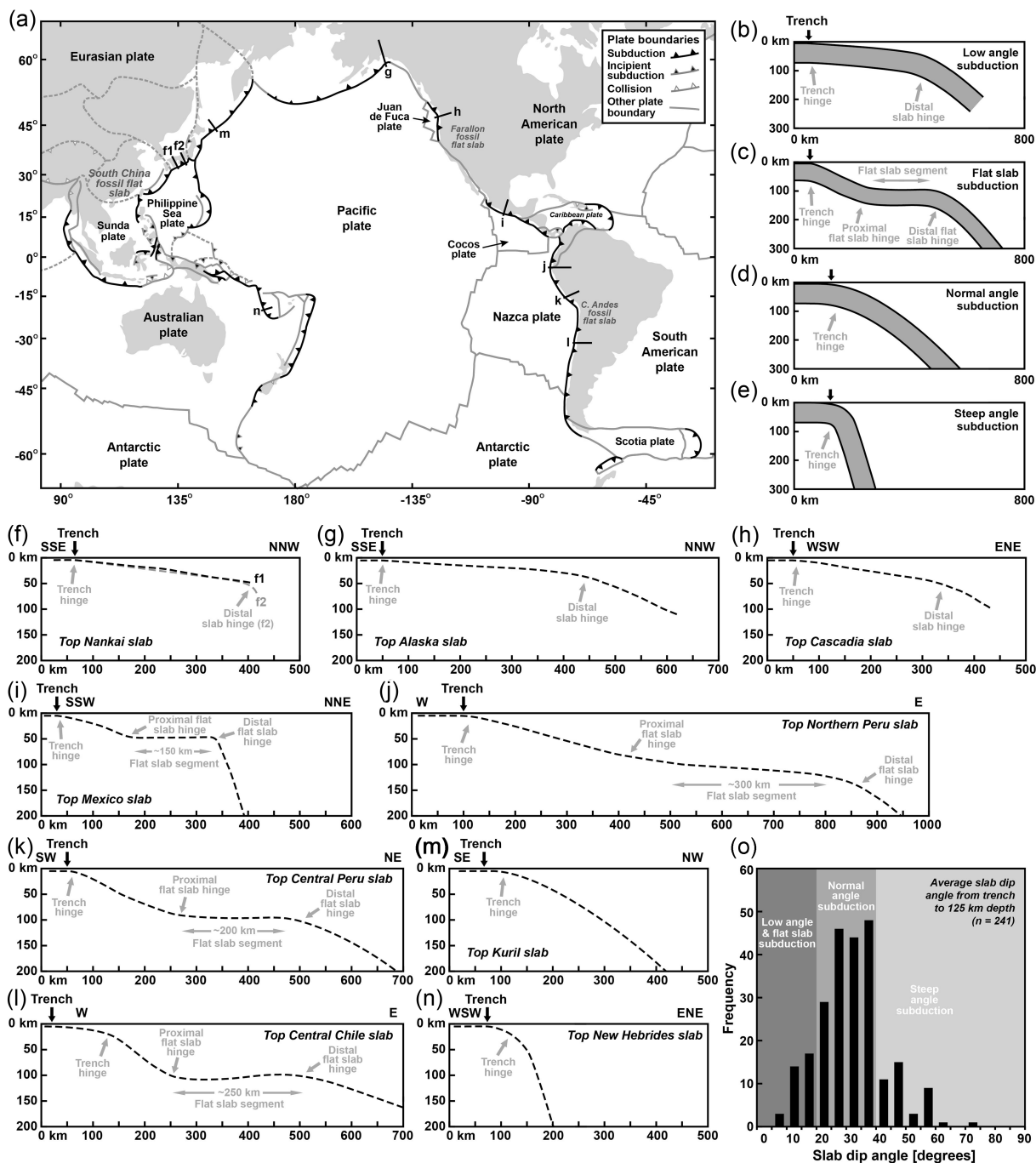


Figure 1. Classification and occurrence in nature of low-angle and flat slab subduction. (a) Tectonic map of the Pacific and Indian Ocean domains showing most active subduction zones on Earth (not shown are the Mediterranean and Makran subduction zones). (b–e) Classification of shallow (from trench to ~200 km depth) subducted slab geometry based on slab dip angle and presence and geometry of slab hinges. (b) Low angle subduction with an average slab dip angle $\leq 20^\circ$ and two subduction hinges (both are convex upward). (c) Flat slab subduction with a flat slab segment dipping $\leq 10^\circ$ and three subduction hinges, of which one is concave upward (proximal flat slab hinge) and two are convex upward (trench hinge and distal flat slab hinge). (d) Normal (intermediate) angle subduction with $20^\circ < \text{average slab dip angle} \leq 40^\circ$ and one subduction hinge (convex upward). (e) Steep angle subduction with an average slab dip angle $> 40^\circ$ and one subduction hinge (convex upward). (f–h) Natural examples of low angle subduction [locations shown in (a)]. (f) Nankai slab segment (geometry from Nakajima & Hasegawa (2007)). (g) Alaska slab segment (geometry derived from Ohta *et al.* (2006)). (h) Cascadia slab (geometry derived from Slab1.0 model (Hayes *et al.* 2012)). (i–l) Natural examples of flat slab subduction [locations shown in (a)]. (i) Mexico slab segment (geometry from Pérez-Campos *et al.* (2008) and Manea *et al.* (2017)). (j) Northern Peru slab segment [geometry derived from Slab1.0 model (Hayes *et al.* 2012)]. (k) Central Peru slab segment (geometry derived from Phillips & Clayton (2014)). (l) Central Chile slab segment [geometry derived from Marot *et al.* (2014)]. (m) Natural example of normal angle subduction, the southern Kuril slab segment [geometry derived from Slab1.0 model (Hayes *et al.* 2012)]. (n) Natural example of steep angle subduction, the southern New Hebrides slab segment [geometry from Slab1.0 model (Hayes *et al.* 2012)]. Panels (g), (k), (m) and (n) have been modified from Schellart (2020). (o) Frequency plot for slab dip angle averaged over a depth range from trench to 125 km depth for 241 subduction segments (~200 km in trench parallel extent) of all active subduction zones on Earth [data updated from Schellart (2008a)]. Note that (f–n) show the geometry of the top of the slab.

characterized by two or three slab hinges in the uppermost 100–200 km. These subduction segments can be subdivided into two categories: subduction with two convex-upward slab hinges and a relatively straight slab segment in between that is dipping at a low angle (Figs 1b, f–h); and subduction involving three slab hinges in the uppermost ~100–200 km of which the middle one is concave upward and the other two are convex upward (Figs 1c, i–l). The former slab geometry with two slab hinges will be referred to as low-angle subduction, considering that the slab in between the two hinges has a low slab dip angle (Fig. 1b). The latter slab geometry, with three slab hinges, will be referred to as flat slab subduction in this contribution, following Schellart (2020), considering that the slab segment in between the second (concave) slab hinge and third (convex) slab hinge lies (sub)horizontally (flat) below the base of the overriding plate (Fig. 1c). The flat slab segment is generally found at 50–150 km depth and extends laterally some 150–300 km in the trench-normal direction for active flat slab subduction settings in nature (Figs 1i–l). This so-called flat slab subduction involving three slab hinges is the subject of this study. Active flat slab subduction is relatively rare on Earth and occurs only in a few localities (e.g. central Chile, central Peru, northern Peru and Mexico, Barazangi & Isacks 1976; Manea *et al.* 2017). Flat slab subduction has also been proposed to have occurred in the geological past (e.g. western North America, southern Peru and East China, Dickinson & Snyder 1978; Bird 1984; Henderson *et al.* 1984; Li & Li 2007; Ramos & Folguera 2009).

1.2 Flat slab subduction, wedge suction and aseismic ridge subduction

Much progress has been made in understanding the origin of flat slab subduction in nature. Early models of subduction zone corner flow pointed to large suction forces in the mantle wedge, reducing the slab dip angle and predicting flat slab subduction for most subduction settings on Earth (Tovish *et al.* 1978). The fact that flat slabs are the exception rather than the rule might suggest that the suction force was overestimated for settings on Earth. Indeed, a low viscosity mantle wedge resulting from, for example, slab dehydration and wedge hydration reduces the suction force, and prevents or reduces flat slab formation, as demonstrated by 2-D subduction models (Manea & Gurnis 2007).

Other work proposed that flat slabs occur through subduction of buoyant ridges or plateaus such as the Juan Fernandez Ridge and Nazca Ridge at the South American subduction zone (Pilger 1981; Henderson *et al.* 1984; Gutscher *et al.* 2000; van Hunen *et al.* 2002; Rosenbaum *et al.* 2005; Liu *et al.* 2010; Antonijevic *et al.* 2015). But geodynamic modelling studies do not provide consistent outcomes, with some studies involving subduction in 2-D space with externally imposed convergence showing flat slab subduction (e.g. van Hunen *et al.* 2002), and others involving buoyancy-driven subduction in 3-D space showing only a limited (~10°) slab dip angle reduction at shallow depth during subduction of large aseismic ridges (e.g. Flórez-Rodríguez *et al.* 2019). Furthermore, the spatial correlation between flat slab and ridge/plateau subduction has many exceptions. Indeed, some flat slab subduction segments lack an aseismic ridge/plateau (e.g. Mexico), and numerous regions of aseismic ridge subduction exist, most notably in the Western Pacific, that lack a flat slab (e.g. Kamchatka with Emperor Ridge, Ryukyu with Amami Plateau and Daito Ridge, Mariana with Marcus-Necker Ridge, New Hebrides with d'Entrecasteaux Ridge, Tonga with Louisville Ridge, e.g. Skinner & Clayton 2011, 2013). It has thus been proposed that

subduction of an aseismic ridge is not sufficient to, by itself, cause flat slab subduction (Antonijevic *et al.* 2015). Indeed, the lack of flat slab subduction (conform Fig. 1c) in the Western Pacific, Indian Ocean, Atlantic Ocean and Mediterranean, including places where a buoyant aseismic ridge or plateau is being subducted, has recently been ascribed to the fact that subduction zones in these regions are either narrow (small trench-parallel extent), young, or both (Schellart 2020), thereby preventing flat slabs to form. Additionally, it was shown that for the present-day flat slabs in the eastern Pacific, their initiation occurred at a time when their subduction zone was wide and old.

1.3 Flat slab subduction during imposed plate or plate boundary motion

Geodynamic modelling studies have reproduced flat slab subduction in cases of forced subduction through externally forced trenchward overriding plate motion and externally forced trench retreat. The imposed overriding plate trenchward velocities vary from 2 to 6 cm yr⁻¹ in several numerical models (e.g. van Hunen *et al.* 2004; Manea & Gurnis 2007; Arcay *et al.* 2008; Gerya *et al.* 2009), while an analogue modelling study uses higher velocities scaling to 9–14 cm yr⁻¹ (Espurt *et al.* 2008). Observed velocities for regions of active flat slab subduction in South and Central America are on the low end of this spectrum or smaller, of the order ~0.7 cm yr⁻¹ (Nazca ridge region), 0.6 cm yr⁻¹ (Mexico flat slab) and 1.6 cm yr⁻¹ (Juan Fernandez flat slab, Schellart *et al.* 2007). These velocities are dependent on the choice of reference frame but in most of these reference frames the velocities are only of the order of a few cm yr⁻¹ or less (Schellart 2008a). The Laramide flat slab likely developed during relatively fast trenchward overriding plate velocities in the range 3–5 cm yr⁻¹ (Liu & Currie 2016).

Other models use imposed convergence velocities of 5–10 cm yr⁻¹, either with a buoyant plateau on the subducting plate (van Hunen *et al.* 2002), with relatively buoyant subducting lithosphere (Shemenda 1993; Gerya *et al.* 2009; Rodríguez-González *et al.* 2012), or with relatively normal oceanic lithosphere (e.g. Olbertz *et al.* 1997; van Hunen *et al.* 2000), forming flat slab subduction during an early phase of subduction. These models might explain the low angle subduction (conform Fig. 1b) as observed in Nankai and Alaska (Figs 1f and g), and proposed for New Guinea, which are relatively young subduction zones. However, the active flat slabs of Central Chile, Peru and Mexico and the proposed past flat slabs in North America (Laramide) and South China have occurred at subduction zones that have been active for more than 100 Myr (Burchfiel & Davis 1975; Coira *et al.* 1982; Collins 2003; Domeier & Torsvik 2014). So for these flat slabs an explanation is needed as to why they formed at a very old subduction zone.

More recently, geodynamic subduction models investigating flat slab subduction have demonstrated that a combination of parameters can create flat slab subduction. For example, forced trench retreat combined with enhanced mantle wedge suction due to a cratonic thick overriding plate (Manea *et al.* 2012), forced trench and plate motion combined with buoyant plateau subduction (Liu & Currie 2016), or forced trench and plate motion combined with buoyant ridge/plateau subduction, young oceanic plate subduction and enhanced mantle wedge suction (Hu *et al.* 2016), can produce flat slab subduction. Antonijevic *et al.* (2015) have also proposed a combination of factors to explain flat slab subduction in Peru, attributing it to subduction of the Nazca ridge, suction and major trench retreat.

1.4 Flat slab subduction in a buoyancy-driven subduction setting

Most geodynamic models discussed above reproducing flat slab subduction have two important aspects in common: (1) they involve forced plate motion and subduction using applied velocity boundary conditions; (2) they do not investigate subduction and flat slab subduction at very long timescales (>100 Myr). A recent work has taken a different approach in which slab flattening and flat slab subduction are studied and reproduced with buoyancy-driven geodynamic models during long-lived subduction (Schellart 2020). It demonstrates that flat slab subduction preferentially occurs in the centre of wide (large trench-parallel extent) subduction zones (as this enhances vertical wedge suction forces) that are very old (active for a long time), because this allows for long-term slab dip angle reduction during progressive subduction into the lower mantle, as a result of strong whole mantle poloidal return flow below the overriding plate. Other recent numerical works presenting 2-D (Yang *et al.* 2019; Strak & Schellart 2021) and 3-D (Schellart 2017) time-evolving buoyancy-driven subduction models concur with the work of Schellart (2020), as they show progressive slab dip angle reduction and early stages of slab flattening (Schellart 2017; Yang *et al.* 2019) or flat slab subduction (Strak & Schellart 2021) in models with significant lower mantle slab penetration and strong whole mantle poloidal return flow below the overriding plate. In the current contribution we build on this approach and test, in a long-term, buoyancy-driven, subduction environment, the effect of a number of physical parameters (overriding plate strength, subducting plate thickness, lower mantle viscosity, inclusion of a plateau) and boundary conditions (free-slip, no-slip and periodic) on the occurrence, duration and mode of flat slab subduction. This leads us to define three modes of flat slab subduction, namely short-lived, long-lived and periodic flat slab subduction. The research also presents a new mechanism, derived from the geodynamic models, to explain the termination of flat slab subduction.

2 METHODS

The numerical geodynamic models have been designed to specifically investigate the long-term evolution of subduction into a deep-mantle reservoir with a particular focus on the evolution of the slab dip angle and the formation of a flat slab. The numerical code *Underworld* is used (Moresi *et al.* 2003, 2007; Stegman *et al.* 2006) to model time-evolving subduction and mantle flow in a rectangular box with compositional buoyancy contrasts in an incompressible Boussinesq fluid. *Underworld* is an open-source numerical particle-in-cell finite element code and is available at <http://www.underworldcode.org>. The models are set up in 2-D space and represent the central region of a wide subduction zone where mantle wedge suction forces are maximum (Dvorkin *et al.* 1993; Schellart 2020). Sets of Lagrangian particles are embedded within a standard Eulerian finite element mesh and represent distinct volumes. The finite element mesh discretises the problem such that the governing equations can be solved. The reader is referred to earlier work (Moresi *et al.* 2003, 2007; Stegman *et al.* 2006; Schellart & Moresi 2013) for detailed information on the numerical method and the equations that are solved.

The models use a 10 000 km long and 2900 km deep (entire mantle depth) rectangular box (Fig. 2). The models include a 660-km-thick upper mantle domain with a non-linear stress-dependent viscosity with a stress exponent $n = 3.5$, a maximum viscosity $\eta_{\text{UM-Max}}$ and minimum viscosity $\eta_{\text{UM-Min}} = 0.1\eta_{\text{UM-Max}}$ following

earlier work to facilitate numerical convergence (Schellart 2017). The models are run non-dimensionally and are later dimensionalized using a length scale ratio (where a non-dimensional length 1 represents 1000 km) and viscosity scale ratio (where a non-dimensional viscosity of 1 represents 5×10^{20} Pa-s) (e.g. Stegman *et al.* 2006; Schellart 2017). The dimensionalized $\eta_{\text{UM-Min}} = 5 \times 10^{19}$ Pa-s and $\eta_{\text{UM-Max}} = 5 \times 10^{20}$ Pa-s, which fall within the estimated range of sublithospheric upper mantle viscosity values in nature (10^{19} – 10^{21} Pa-s, Peltier 2004; James *et al.* 2009; Harig *et al.* 2010). Note that using half of the dimensionalized viscosity values, which is perfectly permissible given the uncertainty in viscosity values in nature, would result in scaled velocity values that are twice as high and scaled time lapses that would be halved.

The upper mantle is underlain by a 2240-km-thick lower mantle with a linear viscosity $\eta_{\text{LM}} = 100\eta_{\text{UM-Max}}$ in most models, including the reference model, following earlier work (Schellart 2017, 2020), and $\eta_{\text{LM}} = 10\eta_{\text{UM-Max}}$ in one model. Studies on the mantle viscosity structure indeed indicate that the lower mantle is about 10–100 times more viscous than the sublithospheric upper mantle (e.g. Hager 1984; Davies & Richards 1992; Davies 1999; Kaufmann & Lambeck 2000). The implemented viscosity step is a reasonable approximation for all the effects of the 660 km discontinuity (viscosity changes, density changes and thermodynamic reactions from mineral phase transitions), as shown in earlier work (e.g. Arredondo & Billen 2016). Apart from the lower mantle viscosity, several other parameters have been tested, namely overriding plate viscosity, subducting plate thickness, inclusion of an oceanic plateau and boundary conditions. The main characteristics of all the models presented and/or discussed in this contribution are presented in Table 1.

The bottom boundary of the model represents the core–mantle boundary, which is modelled in most experiments, including the reference experiment, with a free-slip boundary because the outer core has a viscosity that is many orders of magnitude smaller than that of the overlying lower mantle (e.g. de Wijs *et al.* 1998; Rutter *et al.* 2002; Palmer & Smylie 2005). In two models a no-slip bottom boundary has been tested. The other model boundaries also have free-slip conditions. Two models also tested open periodic boundary conditions.

The primary goal of the current work is to demonstrate the influence of a number of parameters on flat slab subduction in a buoyancy-driven environment for an isolated subduction system. As such, there are no imposed (non-zero) velocity boundary conditions and the large model box and the free-slip boundaries are chosen to reduce the influence of the boundaries on the model outcomes. Mantle flow, subduction, plate motion and plate deformation are driven entirely by buoyancy forces, comparable to earlier models of whole mantle subduction in 2-D space in which the long-term evolution of subduction is investigated (e.g. Zhong & Gurnis 1995).

In the reference model an 80-km-thick three-layer oceanic subducting plate with a strong viscous core is implemented following earlier work (Stegman *et al.* 2010; Schellart 2017), simulating relatively young oceanic lithosphere, comparable to subducting oceanic plates along the west coast of the Americas, with an average age of 40–50 Ma. The top layer is a 30-km-thick viscoplastic layer with a maximum viscosity ($\eta_{\text{SP-T-Max}} = 1000\eta_{\text{UM-Max}}$) and a von Mises rheology that allows for the vertical decoupling of the subducting plate from the free-slip top surface and allows for weak mechanical coupling between the subducting and overriding plates. During subduction, the entire viscoplastic layer yields and shows a viscosity reduction near the trench, but in general the viscosity reduction is often highest in the top part of the layer close to the overriding plate. The yield stress used for the viscoplastic top layer

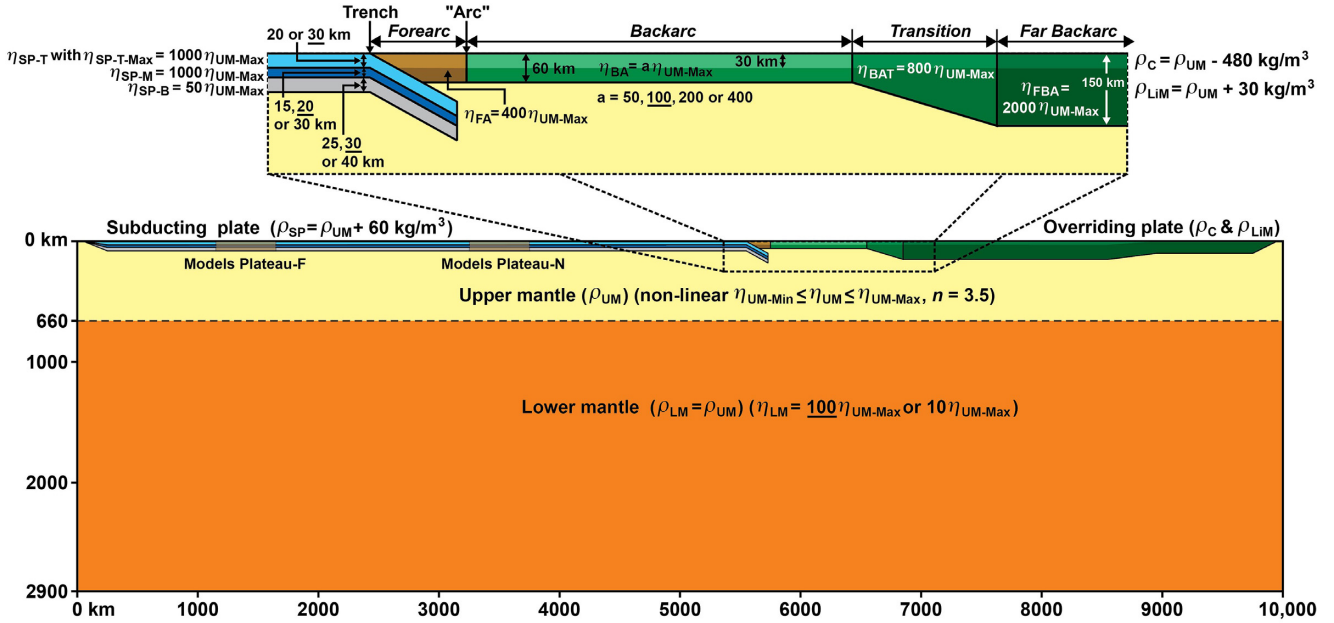


Figure 2. Numerical model set-up to investigate buoyancy-driven time-evolving subduction and flat slab formation in a very large 2-D domain with a layered whole mantle reservoir. The geodynamic model includes a layered negatively buoyant subducting plate with three layers with different viscosity (top, middle and bottom) and a layered overriding plate with two layers with the same viscosity but different density (crustal layer and lithospheric mantle layer). η_{SP-T} = subducting plate top layer viscosity, $\eta_{SP-T-Max}$ = subducting plate top layer maximum viscosity, η_{SP-M} = subducting plate middle layer viscosity, η_{SP-B} = subducting plate bottom layer viscosity, η_{FA} = forearc viscosity, η_{BA} = backarc viscosity, η_{BAT} = backarc transition zone viscosity, η_{FBA} = far backarc viscosity, η_{UM} = sublithospheric upper mantle viscosity, η_{UM-Min} = minimum sublithospheric upper mantle viscosity, η_{UM-Max} = maximum sublithospheric upper mantle viscosity, η_{LM} = lower mantle viscosity, ρ_{UM} = sublithospheric upper mantle density, ρ_{LM} = lower mantle density, ρ_{SP} = subducting plate density, ρ_C = continental crustal density and ρ_{LIM} = continental lithospheric mantle density. Note that those values that are underlined are the values for the reference model. The other values are used for the models of the parametric investigation. See Table 1 and methods for more details.

Table 1. Numerical model parameters.

Model	Subducting plate thickness [km]	Backarc non-dimensional viscosity	Boundary conditions side walls	Boundary conditions bottom	Plateau
BA50	80	50	Free-slip	Free-slip	No
Reference (BA100)	80	100	Free-slip	Free-slip	No
BA200	80	200	Free-slip	Free-slip	No
BA400	80	400	Free-slip	Free-slip	No
SP60	60	100	Free-slip	Free-slip	No
SP100	100	100	Free-slip	Free-slip	No
SP100-BA400	100	400	Free-slip	Free-slip	No
LM10*	80	100	Free-slip	Free-slip	No
NSB_BA100	80	100	Free-slip	No-slip	No
NSB_BA400	80	400	Free-slip	No-slip	No
PSW_BA100	80	100	Periodic	Free-slip	No
PSW_BA400	80	400	Periodic	Free-slip	No
Plateau_N-Buo ^{&}	80	100	Free-slip	Free-slip	Near, Buoyant
Plateau_N-Neu [#]	80	100	Free-slip	Free-slip	Near, Neutral
Plateau_F-Buo ^{\$}	80	100	Free-slip	Free-slip	Far, Buoyant
Plateau_F-Neu [^]	80	100	Free-slip	Free-slip	Far, Neutral
Reference_LowRes [@]	80	100	Free-slip	Free-slip	No
Reference_HighRes [%]	80	100	Free-slip	Free-slip	No

*This model is the same as the reference model except that it has a non-dimensional lower mantle viscosity of 10 rather than 100.

[&]Nearest plateau edge at 1800 km from trench and a buoyant plateau lithosphere that is 37.5 kg m^{-3} less dense than the sublithospheric mantle.

[#]Nearest plateau edge at 1800 km from trench and a plateau lithosphere that has the same density as the sublithospheric mantle.

^{\$}Nearest plateau edge at 3900 km from trench and a buoyant plateau lithosphere that is 37.5 kg m^{-3} less dense than the sublithospheric mantle.

[^]Nearest plateau edge at 3900 km from trench and a plateau lithosphere that has the same density as the sublithospheric mantle.

[@]This model is the same as the reference model except that it has a lower resolution of 512 by 192 elements (instead of 1024 by 512).

[%]This model is the same as the reference model except that it has a higher resolution of 2048 by 1024 elements (instead of 1024 by 512).

scales to 23.5 MPa, which is within the range estimated for large natural subduction zones like the South American subduction zone (Strak & Schellart 2021). The middle layer is 20 km thick and strong with a Newtonian rheology ($\eta_{SP-M} = 1000\eta_{UM-Max}$), while the bottom layer is 30 km thick and also Newtonian but weaker ($\eta_{SP-B} = 50\eta_{UM-Max}$). This gives an effective slab viscosity in the range $\sim 270\eta_{UM-Max}$ to $644\eta_{UM-Max}$, which is comparable to effective viscosities for subducting slabs deduced in previous works (Ribe 2010; Stegman *et al.* 2010). Furthermore, the rheological layering of the subducting plate represents a first-order approximation of a strength profile for oceanic lithosphere with a brittle top part, a strong (high-viscosity) centre and a weak (low-viscosity) bottom (Schellart & Strak 2016). Note that the rheology of the subducted slab remains constant and is independent of its depth, following earlier works (e.g. Stegman *et al.* 2006, 2010). The subducting plate is 60 kg m^{-3} denser than the sublithospheric mantle and is laterally homogeneous, except for those models with an oceanic plateau. It is 5500 km long at the surface with a 200-km-long tapered trailing edge, and has an additional initial slab perturbation dipping at 29° with a length of 206 km. Additional models were run with a greater and smaller subducting plate thickness (SP60 and SP100, with a total thickness of 60 and 100 km, a 20 and 30 km top layer, 15 and 30 km middle layer and 25 and 40 km bottom layer, respectively) to test the influence of the subducting plate thickness on flat slab subduction.

The overriding plate is 4400 km long and its thickness varies in the trench-normal direction (Fig. 2) following earlier work on the geometry of continental overriding plates bordering Pacific subduction zones (Currie & Hyndman 2006). It contains a continental part and a trailing oceanic part that together make a large overriding plate comparable to plates such as the South American and North American plates. The continental region contains a Newtonian viscous forearc with a 200 km length and Newtonian viscous backarc with an 800 km length that are both 60 km thick. The forearc viscosity and backarc viscosity for the reference model are $\eta_{FA} = 400\eta_{UM-Max}$ and $\eta_{BA} = 100\eta_{UM-Max}$, respectively. Other models were run with a different backarc viscosity (BA50 with $\eta_{BA} = 50\eta_{UM-Max}$, BA200 with $\eta_{BA} = 200\eta_{UM-Max}$, BA400 with $\eta_{BA} = 400\eta_{UM-Max}$) to test the influence of the overriding plate strength on flat slab subduction and the duration thereof. An additional model was also run that includes both a greater subducting plate thickness (100 km) and a higher backarc viscosity ($\eta_{BA} = 400\eta_{UM-Max}$) (model SP100-BA400). The backarc is followed by a 300-km-long, Newtonian viscous, transition zone ($\eta_{BAT} = 800\eta_{UM-Max}$) with a thickness increasing from 60 to 150 km, and a 3100-km-long far backarc region with Newtonian viscosity ($\eta_{FBA} = 2000\eta_{UM-Max}$) that has a 2100-km-long, 150-km-thick, continental part and a trailing oceanic region that is 1000 km long and 100 km thick but includes a 200-km-long tapered trailing edge. The continental part includes a 30-km-thick crustal layer that is 480 kg m^{-3} less dense than the sublithospheric mantle. Finally, the overriding plate lithospheric mantle is 30 kg m^{-3} denser than the sublithospheric mantle.

The tapered trailing edges of both the subducting plate and the overriding plate mimic the relatively free plate boundary of a spreading ridge, as adopted in earlier models (Stegman *et al.* 2010; Schellart & Moresi 2013). These edges are thus relatively passive boundaries in that they do not add to the drive of plate motion (nor do they resist plate motion), in agreement with the general concept that spreading ridges are passive features (e.g. Davies & Richards

1992; Davies 1999) and play only a subordinate role in driving plate tectonics (Forsyth & Uyeda 1975).

The same approach is followed as Stegman *et al.* (2006, 2010) in which the models are isothermal and thermochemical convection in the Earth is modelled with chemical convection only such that density contrasts are externally imposed and non-diffusing. The absence of thermal gradients will affect the upper mantle slab viscosity and slab-upper mantle density contrast, which will be higher in these models than in models that include thermal gradients. Due to the high upper mantle slab sinking rates, however, these thermal effects do not have any significant effect on the subduction evolution. Lower mantle slab warming is expected to be more significant than upper mantle slab warming due to the slower sinking velocities in the lower mantle, producing a weaker slab in the lower mantle, thereby resulting in stronger slab folding with tighter slab fold structures in the lower mantle (Strak & Schellart 2021). However, the density contrast between the ambient mantle and lower mantle folded slab pile, which includes the slab and the entrained mantle material enclosed within the slab folds and which sinks as one entity, is not significantly affected, as the warming of the folded slab coincides with the cooling of the entrained mantle material enclosed within the folds (Schellart 2017). Thus, the entire folded slab pile's thermal buoyancy contrast is not diminished on a timescale of 100–200 Myr, and so the lower mantle slab driving mechanism is not significantly affected (Strak & Schellart 2021). A consequence of the isothermal conditions in our models is that they cannot develop a cold mantle wedge corner that might form due to cooling by the cold slab below, which would imply, locally, a higher viscosity. However, dehydration of the slab causes water to infiltrate the mantle wedge corner, which would reduce the mantle wedge corner viscosity (e.g. Manea & Gurnis 2007), countering the effect of a higher viscosity due to a temperature reduction.

Apart from testing the influence of subducting plate thickness and overriding plate strength on subduction evolution and flat slab development, four models have been run to investigate the presence of a buoyant oceanic plateau on the subduction evolution and its effect on the evolution of the slab dip angle in a buoyancy-driven subduction environment. In all cases the plateau has a length of 500 km and an average density is implemented for the entire lithospheric thickness such that lithospheric density contrast with the underlying mantle is -37.5 kg m^{-3} (i.e. lighter than the underlying mantle) or 0 kg m^{-3} (i.e. same density as the underlying mantle). Additionally, the nearest edge of the plateau is located either 1800 km from the trench or 3900 km from the trench to test the influence of plateau subduction in a younger and older subduction system (Fig. 2 and Table 1).

The $10\,000 \times 2900 \text{ km}$ numerical domain has a standard resolution of 1024 (length) by 512 (depth) elements for all the models except for those models with a buoyant plateau, for which a higher resolution of 2048 by 1024 was used. For the reference model, tests were also run at low resolution of 512 by 192 elements and high resolution of 2048 by 1024 elements. These are briefly described in Appendix A. A spatially adaptive mesh has been implemented such that a domain of 3000 km (length) by 290 km (depth) around the subduction zone has a maximum resolution with cells with spatial dimensions of 4.9 km (length) by 2.8 km (depth) (and half these dimensions for the highest resolution) to resolve the subduction zone interface at relatively high resolution for this type of simulation. Initial particle distribution is 20 particles per cell. The models at standard resolution would generally run for 4000–5000 time steps.

3 RESULTS

In the following three subsections the results of the reference model will be described. In the last five subsections of the results section the influence of the backarc viscosity, subducting plate thickness, oceanic plateau subduction, lower mantle viscosity and boundary conditions will be described.

3.1 Subduction kinematics

The reference model starts with transient free sinking of the slab in the upper mantle during which the subducting plate velocity (v_{SP}), overriding plate velocity (v_{OP}), trench velocity (v_T) and subduction velocity (v_S) increase to a maximum just before the slab tip approaches the 660 km discontinuity. This is followed by a sharp decrease when the slab tip first touches the 660 km discontinuity, which marks the last part of the upper mantle subduction phase, and then an increase during the transition phase when a first fold forms at the 660 km discontinuity. During the transition phase and the following phase of whole mantle subduction, the velocities generally show periodic behaviour with a periodicity of ~ 20 Myr that coincides with periodic slab folding at the discontinuity (Figs 3 and 4a–d). The start of the whole mantle subduction phase is marked by sinking of the folded slab pile into the lower mantle. The same periodicity is observed in the horizontal deviatoric normal stress (σ_{XX}) in the subducting plate (Fig. 4i), where the maxima and minima in σ_{XX} closely coincide with the maxima and minima in v_{SP} , v_S and v_{SP}/v_S . This indicates that an increase in slab pull corresponds with an increase in subducting plate velocity, subduction velocity and subduction partitioning. During the upper mantle subduction phase, which lasts until ~ 40 Myr, subduction is roughly equally partitioned between trench retreat and trenchward subducting plate motion (Fig. 4d). During the following transition phase and whole mantle subduction phase, subduction is mostly accommodated by trenchward subducting plate motion. Overriding plate deformation starts with two extension periods during the upper mantle and transition phases with a maximum extension rate of 1.2 cm yr^{-1} (Fig. 4b) and finite extension exceeding 200 km (Fig. 4e). Extension is followed by overriding plate shortening from ~ 53 Myr onwards during whole mantle subduction with an overall increase in shortening rate until ~ 130 Myr reaching -1.0 cm yr^{-1} , superposed on which is a periodic variability, followed by a decreasing shortening rate until the end of the model run reaching -0.5 cm yr^{-1} (Fig. 4b). Finite shortening of the entire overriding plate at the end of the model run is in excess of 400 km (Fig. 4e).

3.2 Evolution of the slab dip angle and flat slab subduction

For the reference model, the shallow slab dip angle (δ_s , averaged over a depth range of 50–200 km) increases to $\sim 54^\circ$ during the first ~ 16 Myr, after which it decreases to a minimum of $\sim 19.5^\circ$ at 130–143 Myr, followed by an increase to $\delta_s = 25^\circ$ at ~ 163 Myr (Fig. 4f). Periodic variability in slab dip angle is superimposed on the long-term decrease and coincides with the periodicity in subduction kinematics and slab folding at the 660 km discontinuity. For the first ~ 109 Myr, the uppermost ~ 300 km of the slab has a convex upward curvature. Then, at ~ 109.4 Myr a concave-upward kink develops (this marks the onset of flat slab development). This kink becomes more pronounced with progressive time when a ~ 150 km long slab segment on the downdip side of the kink progressively decreases its dip angle, which eventually evolves into a flat slab segment at ~ 100 – 200 km depth (Figs 3c–d, 4g, 5). At 126–144 Myr the

flat slab segment has a local slab dip angle (δ_f , determined as the minimum slab dip angle for a local, 100-km-long, slab segment within the depth range 100–200 km) ranging between $\delta_f = -2^\circ$ and 10° (dark grey zone in Figs 4a–i), while trench migration rates are very small (-0.2 to 0.2 cm/yr), and the subducting plate velocity and subduction velocity reach a broad local minimum (Figs 4a and d). During the last ~ 20 Myr of the simulation the slab generally straightens, except for a brief period at ~ 152 – 158 Myr when $\delta_f = 9$ – 10° , causing the flat slab to disappear, attaining a dip $\delta_f = \sim 22^\circ$ at the end of the simulation (Figs 4f and g).

In the reference model overriding plate extension during the upper mantle and transitional subduction phases coincides with a relatively steep slab dip angle and tensional deviatoric stresses in the overriding plate, while the following phase of overriding plate shortening from 53 Myr onwards during whole mantle subduction is characterized by an, on average, much lower slab dip angle and compressive deviatoric stresses in the overriding plate (Figs 3a,c, 4b, f and 5g). After the peak shortening rate at ~ 130 Myr, the latest stage of slab flattening from $\delta_f = 4^\circ$ to -2° (Fig. 4g) coincides with a drop in shortening rate from -1.0 to -0.5 cm yr^{-1} (Fig. 4b) and a decrease in compressive stresses in the overriding plate, which are maximum at the onset of flat slab subduction but are lower when the flat slab is maximum (Fig. 5g).

3.3 Wedge tip evolution, wedge suction and basal compression

In the reference model, a concave upward slab kink first appears at ~ 100 km depth at ~ 109.4 Myr. This time marks the onset of slab flattening in the model and coincides with a sharp decrease in the mantle wedge tip angle (α), as can be seen for the reference model with $\alpha = 52^\circ$ at 108 Myr, dropping to 8° at 132–135 Myr (Fig. 4h). To investigate the role of the mantle surrounding the slab, we are interested in the vertical normal traction components on the slab top surface and bottom surface that deviate from the lithostatic pressure, namely the deviatoric stress σ_{YY} . In case σ_{YY} is tensile at the top surface of the slab (i.e. wedge suction) and σ_{YY} is compressive at the bottom of the slab (basal compression), then these stresses provide a lifting force that promotes flat slab subduction. Although the magnitude of σ_{YY} in the mantle wedge just above the top of the slab is comparable (and tensional) in an early (Fig. 6a) and more advanced stage (Fig. 6b) of subduction, σ_{YY} in the subslab region just below the slab base is more compressive in the advanced stage. Moreover, the decrease in α enhances the effective vertical wedge suction force due to the lowering of the dip angle, thus promoting flat slab development (Fig. 4g). At the start of flat slab subduction, just before the wedge tip angle reaches its minimum, vertical deviatoric normal stresses reach values up to 5 MPa (tension) in the mantle wedge tip and at the slab top surface, and -2 to 0 MPa (compression) at the base of the slab (Fig. 6b). In a late stage of flat slab subduction and during flat slab removal α rapidly increases, reaching 59° at the end of the experiment (Fig. 4h). During flat slab removal, σ_{YY} and vertical wedge suction forces are generally relatively low (Fig. 6c), significantly lower than during flat slab formation (Fig. 6b).

3.4 Influence of overriding plate strength

For those models with a different backarc viscosity (Fig. 7), the evolution of the slab dip angle is comparable to the reference model for the first ~ 100 Myr, showing a long-term decrease of δ_s and δ_f , with, superposed on this, a periodic variability (Fig. 8). During the onset

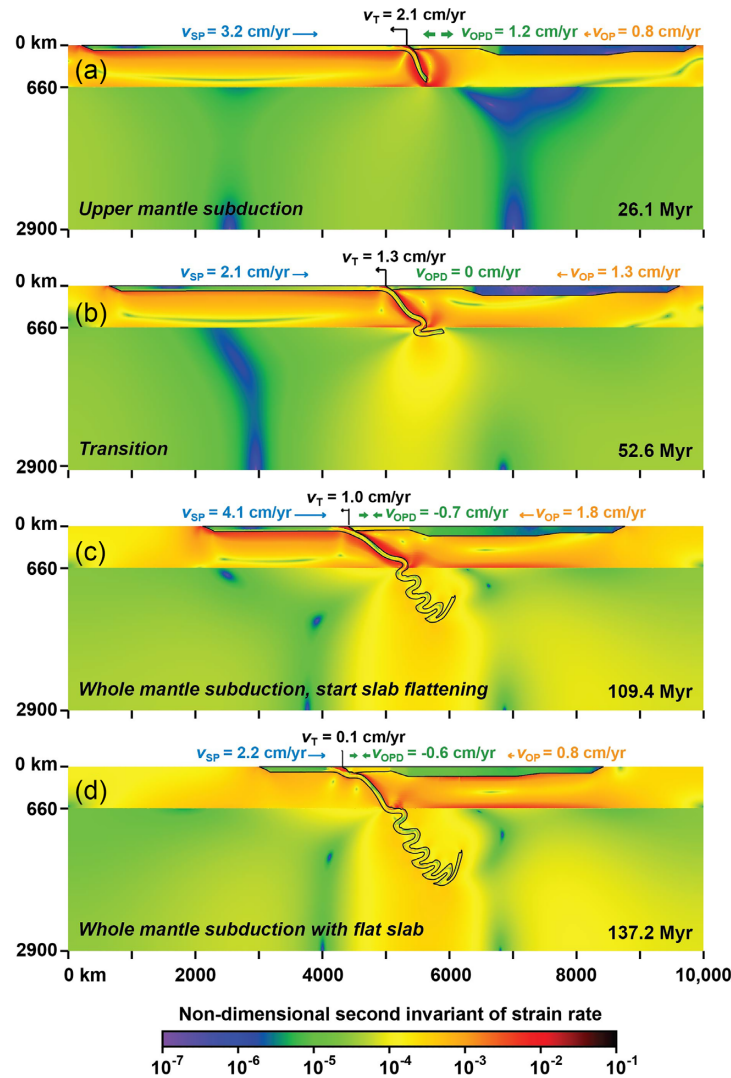


Figure 3. Numerical results of the reference model showing the progressive evolution of subduction in cross-section. (a) Upper mantle subduction stage. (b) Transition from upper mantle to whole mantle subduction stage. (c) Advanced stage of whole mantle subduction and start of slab flattening (first occurrence of concave-upward flat slab hinge). (d) Flat slab subduction during advanced stage of whole mantle subduction. The colours illustrate the non-dimensional strain rate field (second invariant of the strain rate tensor). Note that the subducting plate, slab and overriding plate are indicated by a black outline. The subducting plate velocity (v_{SP} , trenchward is positive), trench velocity (v_T , retreat is positive), overriding plate deformation rate (v_{OPD} , extension is positive) and overriding plate velocity (at the trailing edge) (v_{OP} , trenchward is positive) are also indicated.

of slab flattening at ~ 100 – 110 Myr, as the third, concave-upward, hinge starts to form, the evolution of the models starts to differ. Those models with a strong backarc (BA200 and BA400) show a much longer period of flat slab subduction (either periodic or continuous until the end of the model run, ≥ 65 and ≥ 75 Myr, respectively) than those with a weaker backarc (BA50 and reference model with a backarc viscosity of 100, 6 and 18 Myr, respectively). All models show that during flat slab subduction, δ_f changes continuously between -4° and 10° (white circles with black outline in Fig. 8), while δ_s remains very stable, changing at most 1° or 2° (black circles in Fig. 8). Of particular interest is the periodicity (on a ~ 20 Myr time scale) in δ_f observed during flat slab subduction, best developed in model BA400, but also observable in model BA200. For model BA400 δ_f remains $\leq 10^\circ$ such that the phase of flat slab subduction is continuous (Fig. 8g). For Model BA200 δ_f exceeds 10° for two brief periods (Fig. 8e), and thus this simulation presents a periodic style of flat slab subduction. In the reference model, a concave upward slab curve first appears at ~ 100 km depth at 109.4 Myr, while

in the other models it occurs at a comparable time (~ 111 Myr for BA50, ~ 100 Myr for BA200, ~ 98 Myr for BA400). The four models all experience overriding plate shortening during slab flattening and flat slab subduction, and all show a general drop in v_{SP} and v_T values and a decreasing shortening rate during progressive flat slab subduction. Overriding plate extension rates and shortening rates decrease with increasing backarc viscosity. Furthermore, the periodicity in deformation rate becomes progressively less pronounced with increasing backarc viscosity (green lines in Figs 8b, d, f and h).

3.5 Influence of subducting plate thickness

For the models with a different subducting plate thickness (60 km for SP60, 100 km for SP100), the evolution of the slab dip angle is comparable to the reference model (80 km thickness) for the first period of normal subduction, showing a long-term decrease of

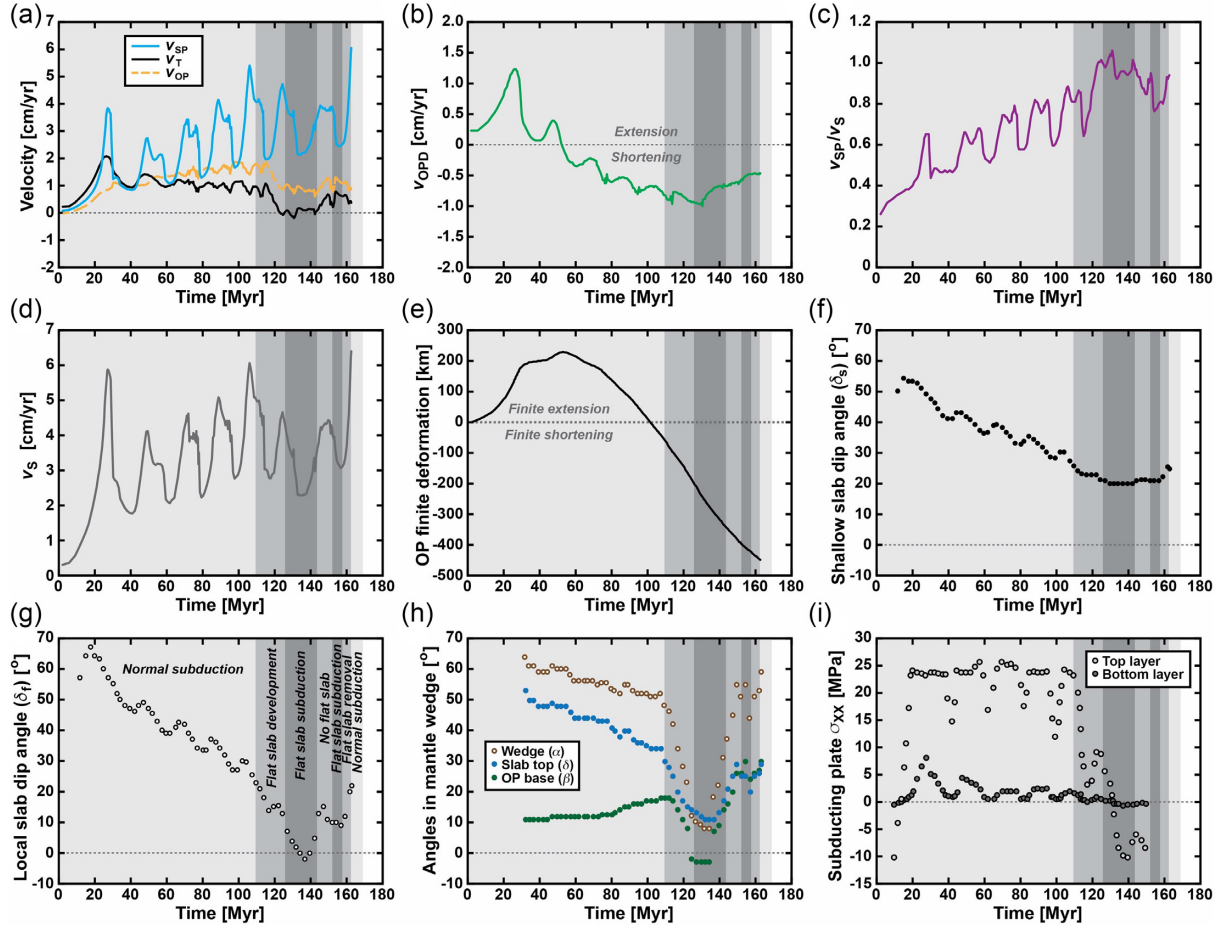


Figure 4. Numerical results of the reference model showing the temporal evolution of subduction zone kinematics, plate motion, overriding plate deformation, slab dip angle, flat slab angle, mantle wedge tip angle and subducting plate stress. (a) Trench-normal subducting plate velocity (v_{SP} , trenchward is positive), trench velocity (v_T , retreat is positive) and overriding plate velocity measured at the trailing edge of the plate (v_{OP} , trenchward is positive). (b) Overriding plate deformation rate ($v_{OPD} = v_T - v_{OP}$, extension is positive). (c) Subduction partitioning ratio (v_{SP}/v_S). (d) Subduction velocity ($v_S = v_T + v_{SP}$). (e) Trench-normal finite deformation of the overriding plate (extension is positive, shortening is negative). (f) Average slab dip angle at 50–200 km depth (δ_s). (g) Minimum slab dip angle for a local, 100-km-long, slab segment within the depth range 100–200 km to determine the flat slab subduction stage (δ_f). (h) Angle (α) of mantle wedge tip, measured from the tip until a vertical opening distance of 20 km; α is the sum of the dip angle δ of the slab top and the dip of the overriding plate base β . (i) Horizontal deviatoric normal stress (σ_{xx}) in the subducting plate top layer and bottom layer measured at 400 km distance from the trench. Note that the dark grey zones indicate periods of flat slab subduction, defined as the time when $\delta_f \leq 10^\circ$. Grey zones indicate times when the slab has three hinges within the depth range 0–200 km but $\delta_f > 10^\circ$. Light grey zones indicate times of normal subduction (only one subduction hinge within the 0–200 km depth range). Also note that α , β and δ are graphically illustrated in Fig. 15.

δ_s and δ_f , with, superposed on this, a periodic variability (Fig. 9). There is a difference in duration of this period, however, lasting ~ 109 Myr for the reference model and ~ 100 Myr for SP100, but lasting nearly 180 Myr for SP60. The slab flattening phase for model SP60 lasts relatively long (~ 44 Myr) compared to the reference model (~ 17 Myr), while that of model SP100 lasts only ~ 4 Myr (cf. Figs 9c, d and 8c). The same is true for the flat slab phases, which last the longest for SP60 (~ 25 Myr), the shortest for SP100 (two short phases of ~ 7 and ~ 4 Myr) and ~ 18 Myr (and one brief phase of 6 Myr) for the reference model. The models show that during flat slab subduction, δ_f changes continuously between -3° and 10° (white circles with black outline in Figs 9c, d and 8c), while δ_s remains very stable, changing at most 1 or 2° (black circles in Figs 9c, d and 8c). Towards the end of the model runs, the flat slab disappears and normal subduction resumes. During slab flattening and flat slab subduction, the shortening rate generally decreases.

3.6 Influence of oceanic plateau subduction

The models that include a positively buoyant plateau (Plateau_N-Buo, Plateau_F-Buo) or neutrally buoyant plateau (Plateau_N-Neu, Plateau_F-Neu) with respect to the sublithospheric mantle evolve in a similar fashion as the reference model right until the plateau reaches the trench. During the plateau subduction stage, the slab dip angle in the upper mantle increases (Figs 10a–c). This dip increase is accompanied by a decrease in the subduction velocity and subducting plate velocity, while the trench velocity becomes negative, that is, the trench starts to advance (Figs 10d–f). For those models with a distant plateau, the slab flattening stage, which starts prior to plateau subduction, is reversed during plateau subduction and the concave-upward slab hinge gradually disappears (Figs 10c2–c4). For the models with a buoyant plateau the slab stretches during plateau subduction, eventually leading to slab detachment and subduction termination before all of the plateau is subducted (Figs 10a4–a5,

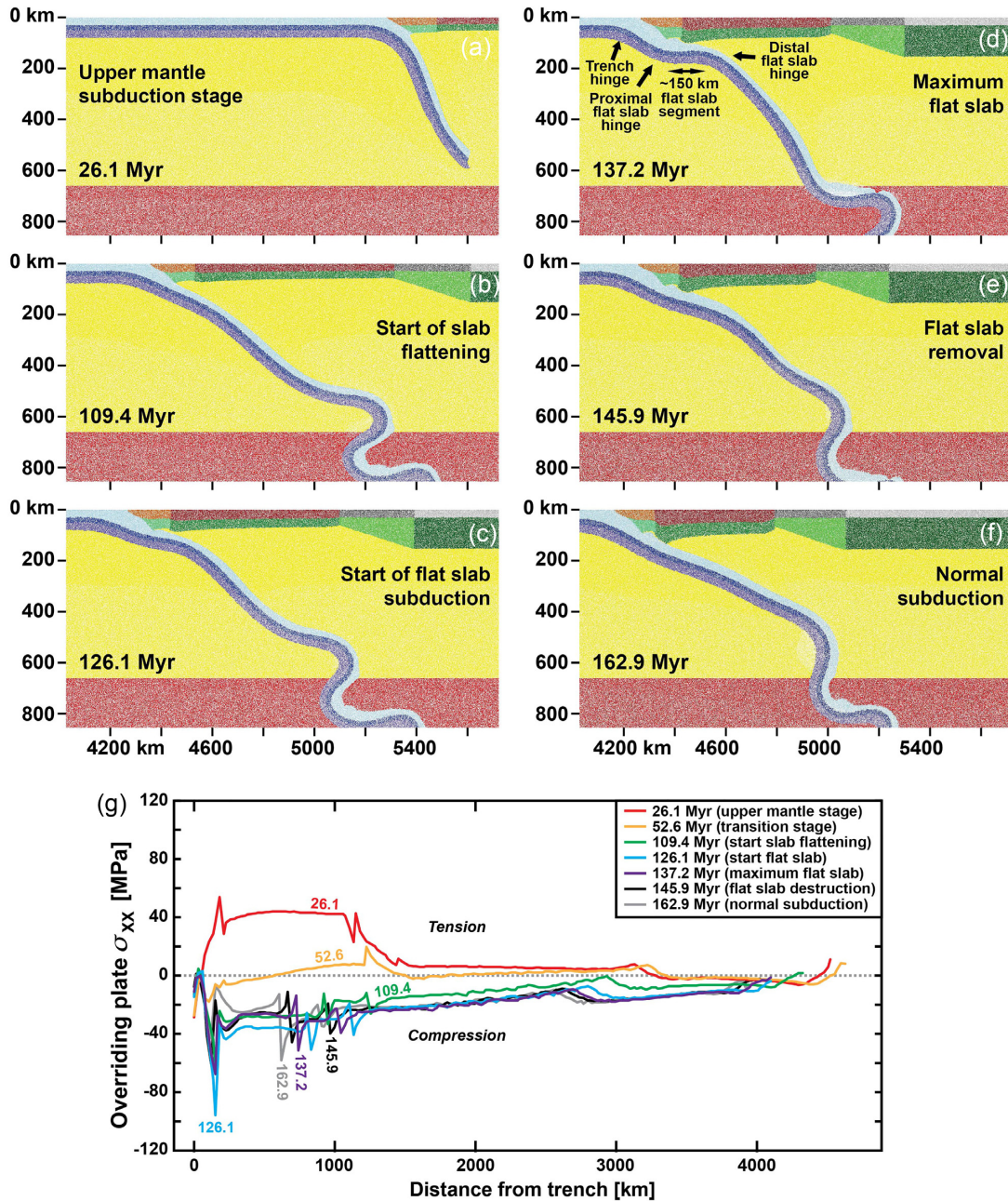


Figure 5. Reference model showing several stages of the progressive evolution of the upper mantle slab geometry before, during and after the flat slab subduction stage and the stresses in the overriding plate. (a) Upper mantle subduction stage. (b) Start of slab flattening with a small concave upward kink in the slab at ~ 100 km depth. (c) Start of flat slab subduction with a more developed concave upward kink. (d) Flat slab subduction with maximum extent of flat slab and minimum flat slab dip angle (-2°). (e) Early stage of flat slab removal. (f) Resumption of \sim normal subduction (concave upward slab hinge has almost disappeared) with a relatively straight slab dipping at a moderate angle. Panels (a)–(f) show the different particle fields. (g) Trench-normal horizontal deviatoric normal stress (σ_{xx}) in the reference model at the overriding plate surface at seven different times (subduction stages for these times are shown in Figs 3, 5). Note that the highest compressive stresses are observed at 126.1 Myr, some 11 Myr before maximum flat slab subduction.

c4–c5). The positive buoyancy of the trailing plateau slab segment then rises to lie flat below the base of the overriding plate. The models with a neutrally buoyant plateau show less stretching and the entire plateau is subducted (Figs 10b4–b5). Once normal subduction resumes, an approximately horizontal slab segment develops at some distance below the base of the overriding plate that includes both oceanic and plateau slab material.

3.7 Influence of lower mantle viscosity

A decrease in lower mantle viscosity to $\eta_{LM} = 10\eta_{UM-Max}$ compared to $\eta_{LM} = 100\eta_{UM-Max}$ for the reference model has a significant effect on the lower mantle slab geometry, plate velocity and trench velocity, but not so much on the uppermost upper mantle slab geometry (Fig. 11). The lower mantle slab shows a rather planar slab geometry, without any slab folding (except for one synform at the

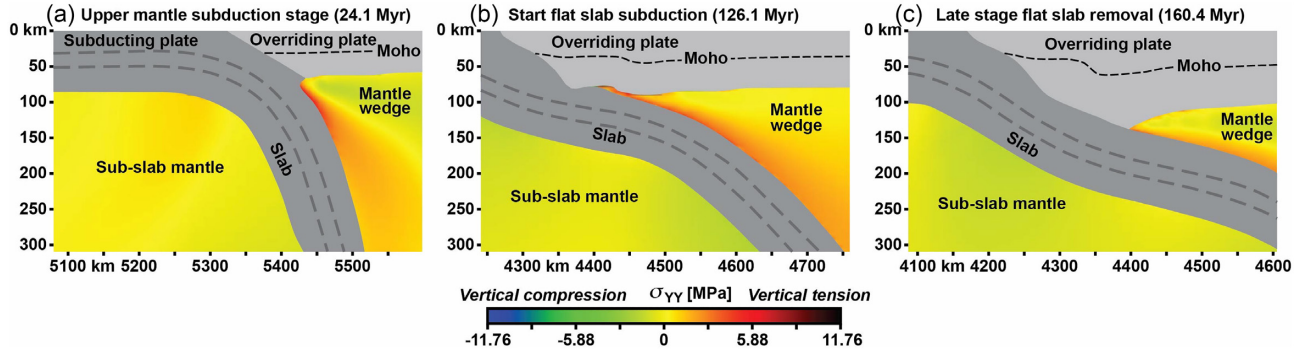


Figure 6. Results of the reference model showing the wedge section in the tip of the mantle wedge and compressive supportive stresses at the base of the slab, as illustrated by the vertical deviatoric normal stress (σ_{YY}), at three different stages during subduction. (a) During the upper mantle subduction stage. (b) At the start of flat slab subduction ($\delta_f \approx 10^\circ$). (c) During an advanced stage of flat slab removal and slab straightening in a late stage of subduction.

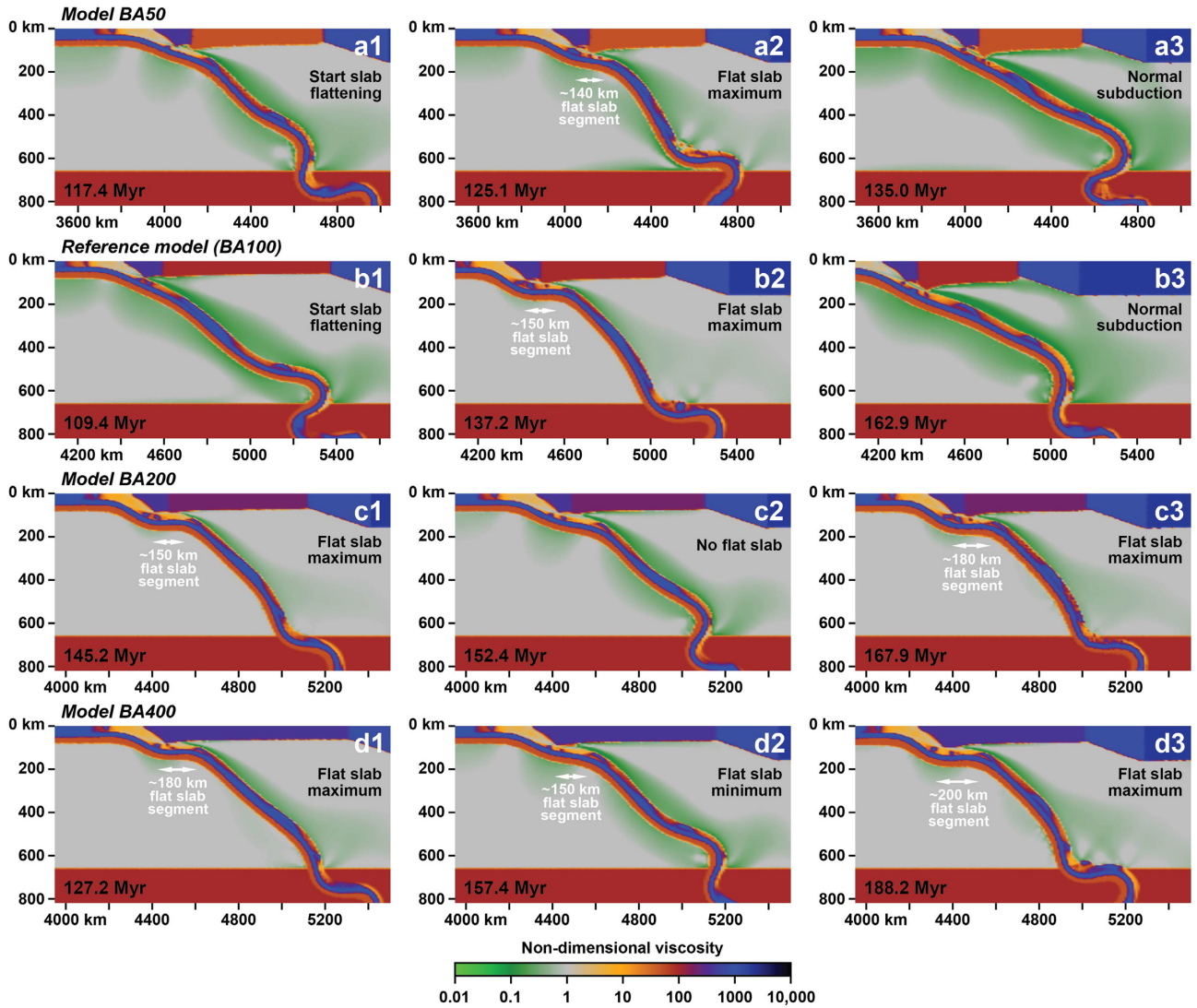


Figure 7. Upper mantle slab geometry for four models with a different backarc viscosity at three stages. (a) Model BA50 with a weak overriding plate backarc ($\eta_{BA} = 50\eta_{UM-Max}$). (b) Reference model with an intermediate strength overriding plate backarc ($\eta_{BA} = 100\eta_{UM-Max}$). (c) Model BA200 with a strong overriding plate backarc ($\eta_{BA} = 200\eta_{UM-Max}$). (d) Model BA400 with a very strong overriding plate backarc ($\eta_{BA} = 400\eta_{UM-Max}$). The cross-sections show the viscosity field, with which the slab geometry can be observed for the four models during a late stage of subduction when flat slab subduction occurs. Note the periodic flat slab subduction in (c) and the periodicity in the flat slab dip angle in (d).

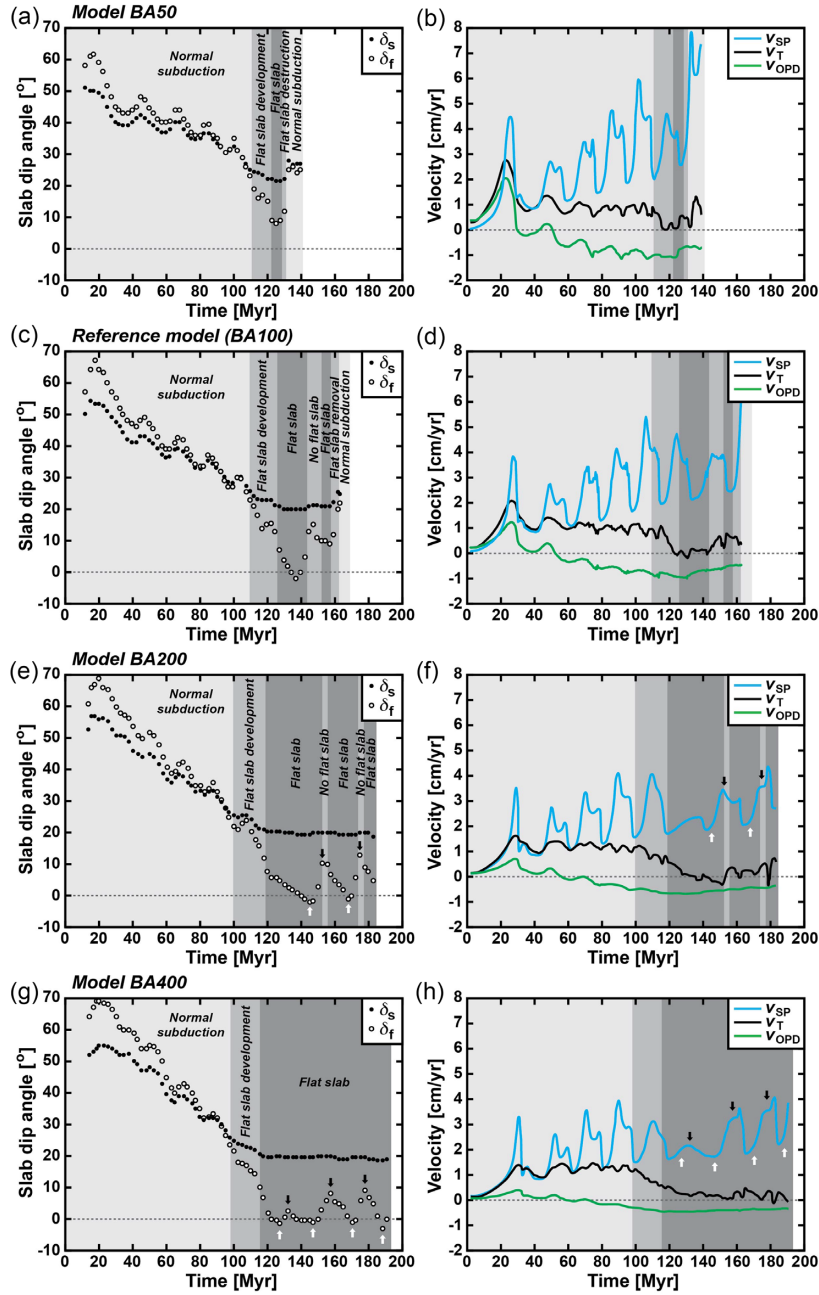


Figure 8. Numerical results for four models with a different backarc viscosity showing (a, c, e, g) the temporal evolution of the average slab dip angle at 50–200 km depth (δ_s) and the local slab dip angle to determine flat slab subduction (δ_f), and (b, d, f, h) the subducting plate velocity (v_{SP} , trenchward is positive), trench velocity (v_T , retreat (oceanward) is positive) and overriding plate deformation rate (v_{OPD} , extension is positive). (a, b) Model BA50 with a weak overriding plate backarc ($\eta_{BA} = 50\eta_{UM-Max}$). (c, d) Reference model with an intermediate strength overriding plate backarc ($\eta_{BA} = 100\eta_{UM-Max}$). (e, f) Model BA200 with a strong overriding plate backarc ($\eta_{BA} = 200\eta_{UM-Max}$). (g, h) Model BA400 with a very strong overriding plate backarc ($\eta_{BA} = 400\eta_{UM-Max}$). Dark grey zones indicate periods of flat slab subduction, defined as the time when $\delta_f \leq 10^\circ$. Grey zones indicate times when slab has three hinges within the depth range 0–200 km but $\delta_f > 10^\circ$. Light grey zones indicate times of normal subduction (only one subduction hinge within the 0–200 km depth range). First appearance of grey zone [110.6 Myr in (a, b), 109.4 Myr in (c, d), 98.8 Myr in (e, f) and 98.2 Myr in (g, h)] marks the onset of formation of a concave-upward slab bend in the shallow part of the slab (which later becomes the proximal flat slab hinge). Note that for the periodic flat slab subduction in (e) and the periodicity in the flat slab dip angle in (g), the most pronounced flat slab times (lowest dips) and minima (highest dips) are indicated with white and black arrows, respectively.

slab tip), which is very different from the reference model (Fig. 3) and the other models (e.g. Fig. 12), which are all characterized by periodic slab folds in their higher-viscosity lower mantle. In terms of upper mantle slab geometry, model LM10 shows a progressive decrease in δ_s and δ_f , leading to slab flattening at ~40 Myr and

flat slab subduction from ~42 Myr until the end of the simulation (Fig. 11c), similar to the reference model, but there is no periodic variability superimposed on these long-term dip angle trends, nor on the overriding plate deformation rate and subducting plate velocity, in contrast to the reference model. Additionally, slab flattening

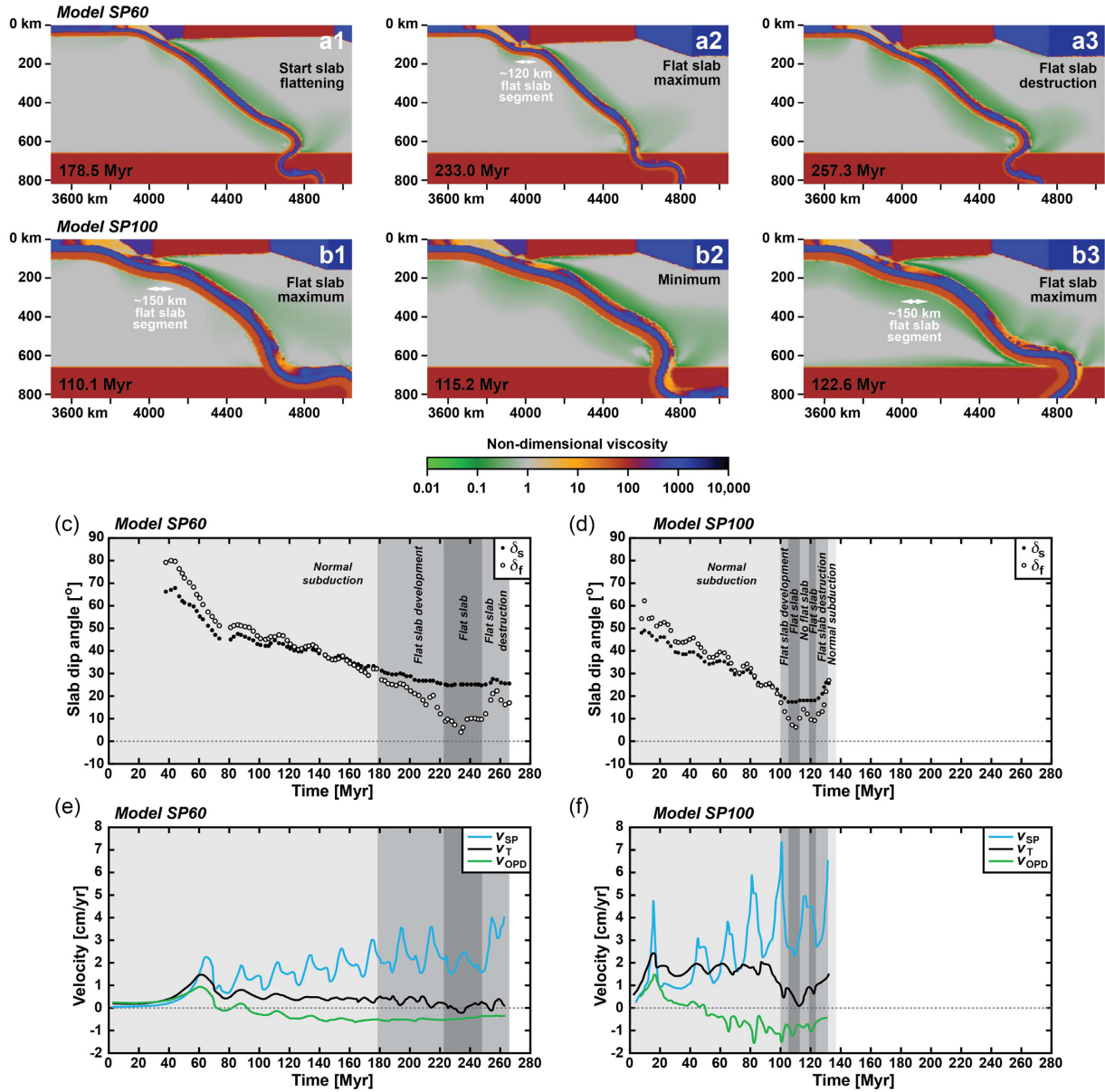


Figure 9. Numerical results for two models with a different subducting plate thickness showing the slab geometry, the temporal evolution of the average slab dip angle at 50–200 km depth (δ_s), the local slab dip angle to determine flat slab subduction (δ_f), and the subduction kinematics. (a, c, e) Model SP60 with a thin subducting plate (60 km). (b, d, f) Model SP100 with a thick subducting plate (100 km). (a–b) Cross-sections showing the viscosity field, with which the slab geometry can be observed for the two models during a late stage of subduction when flat slab subduction occurs. (c–d) δ_s (black circles) and δ_f (white circles with black outline). Dark grey zones indicate periods of flat slab subduction when $\delta_f \leq 10^\circ$. First appearance of grey zone (178.5 Myr in (c) and 100.4 Myr in (d)) marks the onset of formation of a concave-upward slab bend in the shallow part of the slab (which later becomes the proximal flat slab hinge). Note the periodic flat slab subduction in (d). (e–f) Subducting plate velocity (v_{SP}), trench velocity (v_T) and overriding plate deformation rate (v_{OPD}) for models SP60 and SP100.

starts much earlier and flat slab subduction lasts longer than in the reference model (*cf.* Figs 11c and 8c). The trench retreat velocity and subducting plate velocity are generally significantly higher than for the reference model (*cf.* Figs 11d and 8d), and the trench velocity drops significantly during slab flattening and flat slab subduction to become slightly negative (advance) in an advanced stage of flat slab subduction.

3.8 Influence of boundary conditions

Fig. 12 shows the influence of several boundary conditions on the flow field in the mantle and the geometry of the slab, including the occurrence/absence of a flat slab. The reference model, which has free-slip boundaries everywhere and shows the formation of a flat slab in a late stage of whole mantle subduction, is characterized by

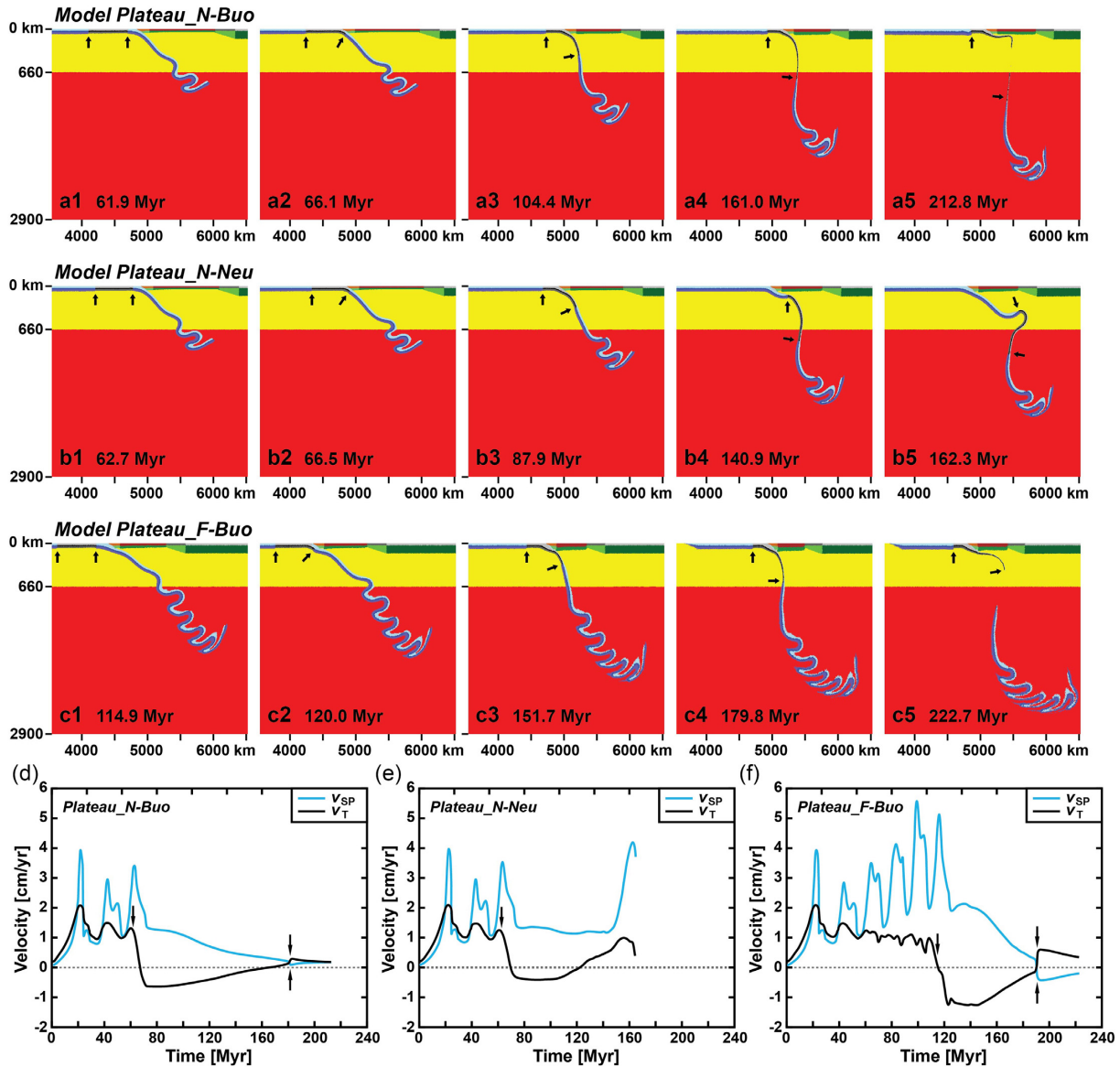


Figure 10. Numerical results for three models that include an oceanic plateau, showing (a–c) the evolution of the slab geometry and (d–f) the evolution of the trench velocity (v_T , retreat (oceanward) is positive) and subducting plate velocity (v_{SP} , trenchward is positive). The cross-sections show the different particle fields, with the plateau edges indicated by black arrows. (a, d) Model Plateau_N-Buo with a positively buoyant plateau (with respect to the sublithospheric mantle) originally located close to the trench. (b, e) Model Plateau_N-Neu with a neutrally buoyant plateau originally located close to the trench. (c, f) Model Plateau_F-Buo with a positively buoyant plateau originally located far from the trench. The single black arrows in (d–f) indicate the time when the leading edge of the plateau starts to subduct. The double black arrows in (d, f) indicate the time when slab detachment occurs. Note the change from trench retreat to trench advance and the reduction in subducting plate velocity soon after plateau subduction commences.

a strong whole mantle poloidal circulation cell below the overriding plate and fast trench-directed upper mantle flow below the overriding plate, which drags the overriding plate trenchward (Fig. 12a). The whole mantle flow cell below the subducting plate is much less pronounced. Model PSW_BA100 with periodic sidewalls and free-slip top and bottom is very similar to the reference model in terms of mantle flow patterns and slab geometry, including flat slab subduction (Fig. 12b), although flat slab subduction does form earlier and after less plate subduction. Model NSB_BA100 with a no-slip bottom boundary and free-slip boundaries elsewhere is different from the reference model in terms of mantle flow field and upper mantle slab geometry. The whole mantle flow cell below the overriding plate

has comparable velocities to the cell below the subducting plate, in particular in the lower mantle. Also, although the streamlines in the location of the lower mantle slab have a comparable range of dip angles for the no-slip-bottom model ($\sim 52\text{--}79^\circ$) and reference model ($\sim 52\text{--}77^\circ$), the lower mantle velocities are much lower in the former (*cf.* Figs 12c and a). Furthermore, the trench-directed upper mantle flow below the overriding plate is much slower compared to the reference model. Flat slab subduction does not develop in model NSB_BA100 (nor in model NSB_BA400), and the start of slab flattening (formation of the concave-upward kink) occurs much later (~ 148.3 Myr for NSB_BA100) than in the reference model (109.4 Myr).

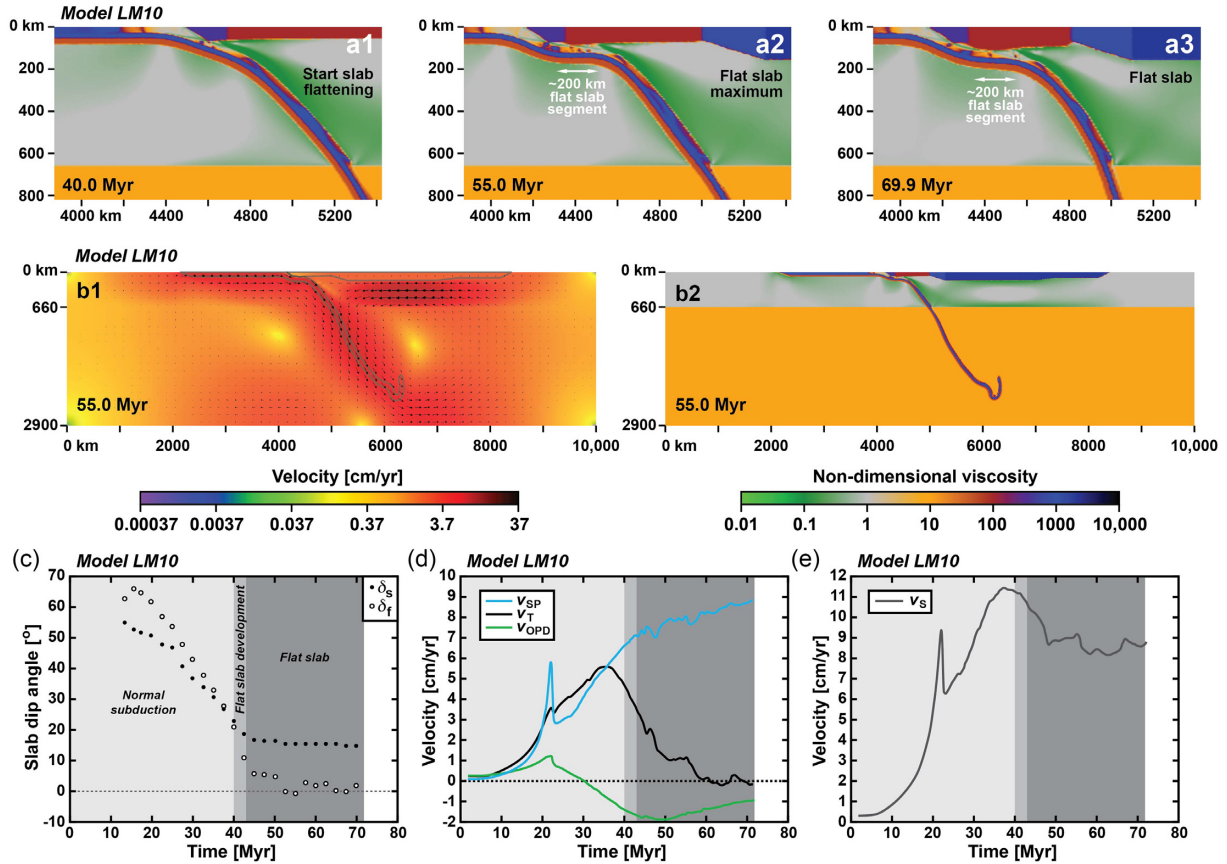


Figure 11. Numerical results for model LM10 that includes a relatively low viscosity lower mantle ($\eta_{LM} = 10\eta_{UM-Max}$ instead of $100\eta_{UM-Max}$ for the reference model). (a) Three cross-sections showing the viscosity field in the upper mantle, illustrating the upper mantle slab geometry in an advanced stage of subduction, including slab flattening and flat slab subduction. (b) Cross-sections showing the velocity field (left-hand panel) and viscosity field (right-hand panel) in the entire model domain during an advanced stage of whole mantle subduction including a flat slab. (c) δ_s (black circles) and δ_f (white circles with black outline). Dark grey zone indicates period of flat slab subduction, defined as the time when $\delta_f \leq 10^\circ$. First appearance of grey zone (40.0 Myr) marks the onset of formation of a concave-upward slab bend in the shallow part of the slab (which later becomes the proximal flat slab hinge). (d) Subducting plate velocity (v_{SP} , trenchward is positive), trench velocity (v_T , retreat (oceanward) is positive) and overriding plate deformation rate (v_{OPD} , extension is positive). (e) Subduction velocity ($v_S = v_{SP} + v_T$).

4 DISCUSSION

4.1 Flat slab initiation mechanism

The progressive decrease in slab dip angle and progressive slab flattening in the models results from the resistance of the upper mantle slab segment to roll back in a wide-slab setting, in particular once the slab starts to sink into the lower mantle, and the trenchward motion of the overriding plate (Schellart 2017, Fig. 13). Slab dip angle reduction and slab flattening are further enhanced by mantle wedge suction forces and (minor) subslab vertical compressive forces. The models represent the central part of a wide subduction zone, where relatively strong wedge suction forces can develop due to the large distance of lateral slab edges. The presence of such edges, which allow for lateral, trench-parallel, mantle inflow (Dvorkin *et al.* 1993; Schellart *et al.* 2007), decreases wedge suction and enhances a steep slab dip angle for narrow slabs and near lateral edges of wide slabs (Schellart 2020). Furthermore, the strength of the slab itself periodically promotes lower dip angles due to its resistance to buckle at the 660 km discontinuity, where the formation of a new slab fold results in the upward transmission of compressive buckling stresses through the slab that temporarily support a lower slab dip angle at shallower depth. This explains the

periodic nature of the slab dip angle evolution shown by all models (e.g. Figs 8 and 9) except model LM10, which did not show any slab folding at the 660 km discontinuity (Fig. 11). Evidence for the periodicity of transmission of these compressive buckling stresses can be found in the slab pull stresses in the subducting plate at the surface. Fig. 4(i) shows the evolution of these stresses with time at two depth levels in the subducting plate, one in the viscoplastic top layer and one in the low-viscosity bottom layer. Note that σ_{XX} in the viscoplastic top layer is limited due to the yield stress. These stresses vary periodically with the same periodicity as v_{SP} , v_S , v_{SP}/v_S , δ_s and δ_f . The local minima in σ_{XX} closely coincide with the minima in the dip angles δ_s and δ_f , indicating that at times when the slab buckling stress provides temporary support for a lower dip angle, the upward-transmitted compressive stress is maximum such that the net slab pull stress in the subducting plate at the surface is minimum.

The trenchward motion of the overriding plate is due to a strong basal drag, causing the leading edge of the overriding plate to actively push the subduction zone hinge backward (oceanward), thereby causing a long-term decrease in upper mantle slab dip angle and enhancing wedge suction (Fig. 13). The strong basal drag results from sublithospheric mantle flow that is part of a whole mantle poloidal return flow cell below the overriding plate, which is

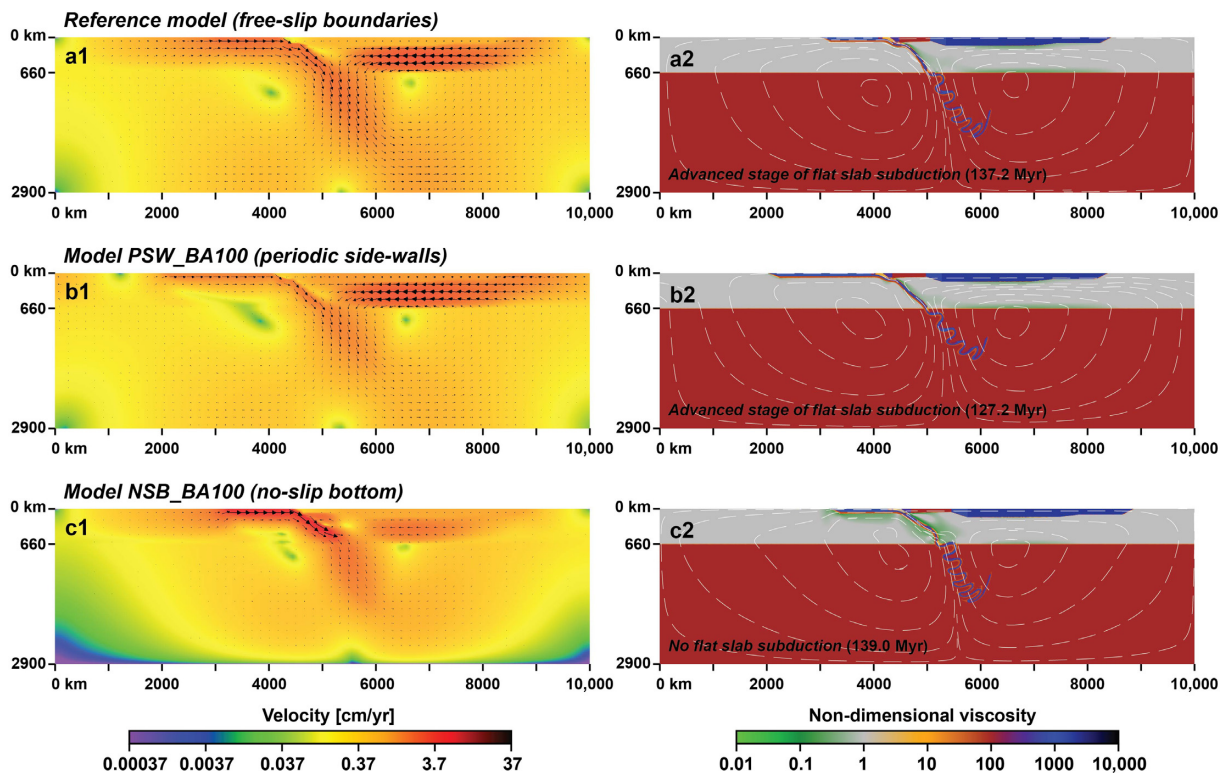


Figure 12. Numerical results for models with different boundary conditions at an advanced stage of whole mantle subduction. (a) the reference model with free-slip boundaries everywhere. (b) Model PSW_BA100, which is the same as the reference model, except that it has periodic side-wall boundary conditions. (c) Model NSB_BA100, which is the same as the reference model except that it has a no-slip bottom boundary condition. Panels on the left-hand side show the velocity field, while panels on the right-hand side show the non-dimensional viscosity field, thereby illustrating the slab geometry, as well as a number of streamlines (white dashed lines).

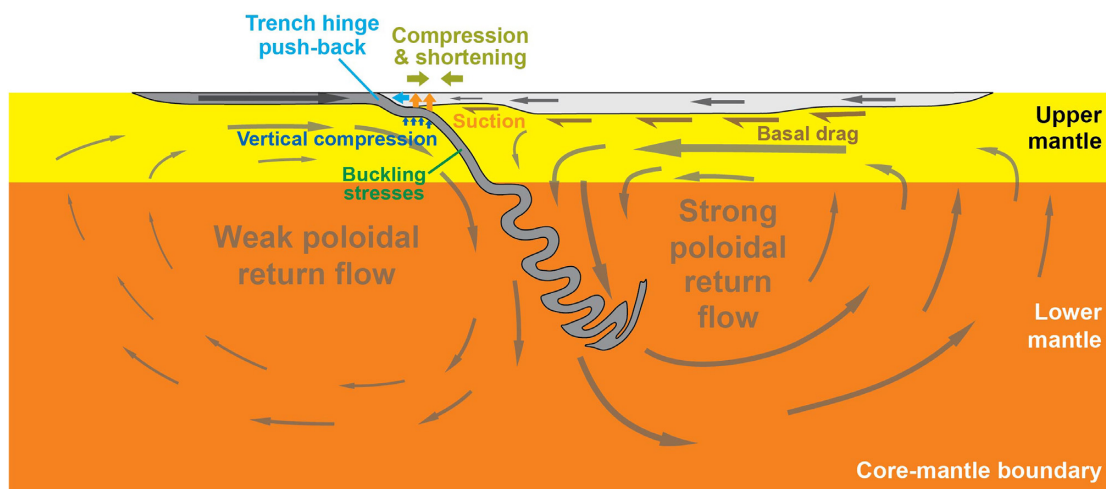


Figure 13. Schematic diagram illustrating the driving mechanism of flat slab subduction and overriding plate shortening during an advanced stage of subduction with the slab extending deep into the lower mantle. This whole mantle subduction drives two poloidal flow cells, one weak cell below the subducting plate and one strong cell below the overriding plate. The strong poloidal cell drives the strong trench-directed flow below the overriding plate, which applies a trench-directed basal drag, and this drag force decreases trenchward, causing the overriding plate to experience trench-normal compression and to move trenchward and push back the trench hinge of the subducting plate, which causes further compression in the overriding plate. Push-back of the trench hinge causes the slab dip angle to decrease, causing the mantle wedge tip to narrow and the mantle wedge suction to increase. Such suction, together with basal compression, promotes flat slab subduction together with slab buckling stresses that form due to folding of the slab at the 660 km discontinuity and the transmission of compressive stresses through the upper mantle slab towards the shallow upper mantle.

induced by the sinking subducting slab (Schellart 2017; Yang *et al.* 2019). The poloidal flow is particularly strong below the overriding plate, and weaker below the subducting plate, because of the asymmetry of subduction in which slab sinking is oriented towards the overriding plate side (Fig. 13). The strength of this return flow cell also depends on boundary conditions (Fig. 12). With a no-slip condition at the core-mantle boundary, the poloidal cell, and with it the return flow in the upper mantle, is much reduced compared to a free-slip boundary, and so slab flattening starts much later and no flat slab subduction develops for the duration of the model run (Fig. 12c), while in the free-slip model it does (Fig. 12a). We note however, that for all models the poloidal return flow would likely have been stronger in case a 3D spherical geometry would have been used, as the return flow path would have been shorter, ultimately leading to faster slab dip angle reductions and faster slab flattening.

Slab folding at the 660 km discontinuity and in the lower mantle has been observed in many previous modelling studies (e.g. Griffiths *et al.* 1995; Guillou-Frottier *et al.* 1995; Christensen 1996; Schellart 2005; Ribe *et al.* 2007; Běhounková & Čížková 2008; Lee & King 2011; Čížková & Bina 2013; Garel *et al.* 2014; Schellart 2017). The current models show that such folding can enhance flat slab subduction. As a buckling instability is supported at its base by the 660 km viscosity step, the buckled slab periodically supports a lower slab dip angle at its top in the uppermost mantle (~ 0 –200 km, Fig. 7) through the mechanical strength of the slab and the resistance to buckling. The upper mantle slab segment thus behaves as a strong beam that can transmit stresses from the 660 km discontinuity to the surface, and can thereby also modulate the slab pull in the subducting plate (Fig. 4i), as discussed earlier. Such behaviour can also be expected for slabs in nature, as slabs have a significantly greater viscosity than the ambient upper mantle, with estimated slab/upper mantle effective viscosity ratios in nature of the order 140–510 (Ribe 2010) or 100–700 (Schellart 2008b), comparable to ratios used in the models (in the range 270–644). Once the slab dip angle has been reduced sufficiently after ~ 100 Myr (Fig. 8), a small decrease in dip angle during a new slab folding phase, together with a relatively high effective suction, can thus lead to flat slab subduction.

If the above-proposed conceptual mechanism would apply to the numerical models (and nature) one would thus expect that slab flattening is dependent on the spatial dimensions of the buckling instability, with a thicker slab likely producing a larger wavelength fold, which would lead to flat slab subduction at an earlier time. This hypothesis is supported by model SP100, with a larger subducting plate thickness (100 km) compared to the reference model (80 km) and model SP60 with a smaller plate thickness (60 km). The results indeed show that flat slab subduction occurs earlier (105 Myr compared to 126 Myr) for a stronger slab (model SP100, Fig. 9d) compared to a weaker slab (reference model, Fig. 8c) and compared to the weakest slab (SP60), which develops a flat slab very late, at ~ 222 Myr (Fig. 9c).

During slab flattening and flat slab subduction, the uppermost ~ 200 km of the slab is characterized by three subduction hinges (Fig. 1c) that impose bending stresses and strains on the slab. Fig. 14 shows model SP100-BA400 with a 100 km thick subducting plate and strong backarc, which has produced a large flat slab. Figs 14(b) and (c) show σ_{xx} and the second invariant of the strain rate in the subducting plate and slab down to 250 km, from which we can deduce that the stresses and strain rates in the different bending zones are reasonably conform to what one would expect given the curvature increases and decreases due to bending, in particular in the strong core layer of the slab, and are in reasonable agreement with

the work of Sandiford *et al.* (2020), for example the 25 Myr panel in their Fig. 6. Nevertheless, some differences arise because other mechanisms are active that also impose stresses and strains on the slab. In particular, shear stresses at the inclined and flat part of the subduction zone interface cause compressive σ_{xx} in the slab close to the interface and in the upper part of the trench hinge zone, which resembles an accretionary wedge-type structure. Other stresses that modulate the system include the slab's negative buoyancy and the upward-transmitted stresses due to periodic buckling. The flat slab segment shows downdip tensile stresses in the uppermost ~ 50 per cent of the strong core layer, mostly downdip tensile stresses in the upper layer of the slab, and downdip compressive stresses in the bottommost ~ 50 per cent of the core layer and the bottom layer (Fig. 14b). Such stresses would thus predict downdip tensile seismicity in the flat slab segment (given that the seismicity is approximately limited to the upper half of the slab), in agreement with the analysis of Sandiford *et al.* (2020).

The geodynamic models demonstrate that flat slab subduction can develop without lateral buoyancy variations in the subducting plate and without externally-driven plate motion or externally-forced trench retreat. During slab flattening v_T decreases and during flat slab subduction v_T is generally slow, between -0.5 and 1.0 cm/yr in models BA50, BA200, BA400, SP60, SP100 and the reference model (Figs 8 and 9). This is different from models with externally imposed trenchward overriding plate motion forcing trench retreat, which show flat slab subduction for retreat rates of 2 – 6 cm yr $^{-1}$ in models with a 2-D spatial set-up (e.g. van Hunen *et al.* 2004; Manea & Gurnis 2007; Arcay *et al.* 2008; Gerya *et al.* 2009) and 9 – 14 cm yr $^{-1}$ for models with a 3-D set-up (Espurt *et al.* 2008). During slab flattening and flat slab subduction, v_{SP} is generally also lower with reduced peak heights and v_{OPD} generally shows a decrease in shortening rate (Figs 8, 9 and 14). The reduced v_{SP} results from the increased subduction interface contact area, and thus larger shear resistance, during slab flattening and flat slab subduction as well as lower slab pull transmitted to the subducting plate (Fig. 4i). The lower v_{SP} gives a lower subduction rate, and with it a slower mantle circulation rate and lower shear drag forces at the base of the overriding plate. This explains why the compressive stresses in the overriding plate are somewhat lower during maximum flat slab subduction than during the start of flat slab subduction (Fig. 5g), and why shortening rates in the overriding plate are lower (Figs 8, 9 and 14).

Flat slab development in the models presented here is supported by a relatively strong suction force in the tip of the mantle wedge (Fig. 6) that dominates over subslab overpressure forces (Fig. 6), in agreement with corner flow models (Tovish *et al.* 1978) and evolutionary subduction models (Manea & Gurnis 2007; Schellart 2020). Earlier work has shown that, apart from the moderate increase in vertical compressive deviatoric stresses at the base of the slab and tensional deviatoric stresses in the tip of the mantle wedge from initial subduction until slab flattening, the effective suction force increases as well due to the gradual decrease in shallow dip angle of the slab (Schellart 2020).

The models further show that, in a buoyancy-driven subduction environment and with a 2-D spatial set-up, subduction of a light or neutrally buoyant plateau does not promote flat slab subduction (Fig. 10). In fact, the models show significant steepening of the slab during plateau subduction, in agreement with results from buoyancy-driven lab experiments in which the buoyant plateau had the same width as the subducting plate (Espurt *et al.* 2008) and buoyancy-driven 2-D numerical models of arc-continent collision and partial continental subduction (Bina *et al.* 2020), but opposite

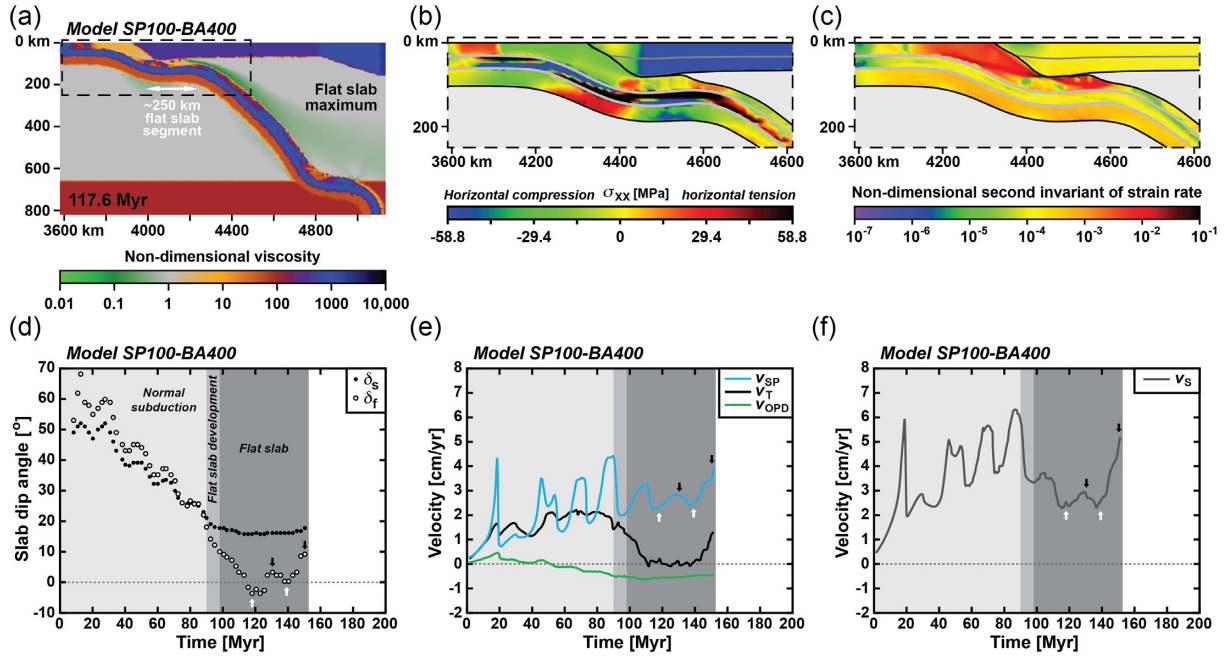


Figure 14. Numerical results for model SP100-BA400 that includes a thick subducting plate (100 km) and a high-viscosity backarc ($\eta_{BA} = 400\eta_{UM-Max}$), showing the slab geometry, stresses, strain rates and the temporal evolution of the slab dip angles and subduction kinematics. (a) Cross-section showing the viscosity field, with which the slab geometry can be observed during a late stage of subduction when the flat slab has its maximum extent. (b,c) Zoom-ins of flat slab region [dashed rectangle shown in (a)] showing the slab and overriding plate trench-normal horizontal deviatoric normal stress σ_{xx} and non-dimensional second invariant of the strain rate, respectively. Note that the grey lines in the slab and subducting plate in (b) and (c) mark the top and bottom boundary of the strong core layer, while the grey line in the overriding plate indicates the Moho. (d) δ_s (black circles) and δ_f (white circles with black outline). Dark grey zone indicates period of flat slab subduction, defined as the time when $\delta_f \leq 10^\circ$. First appearance of grey zone (at 90.3 Myr) marks the onset of formation of a concave-upward slab bend in the shallow part of the slab (which later becomes the proximal flat slab hinge). Flat slab subduction starts at 97.5 Myr. (e) Subducting plate velocity (v_{SP} , trenchward is positive), trench velocity (v_T , retreat (oceanward) is positive) and overriding plate deformation rate (v_{OPD} , extension is positive). (f) Subduction velocity ($v_S = v_{SP} + v_T$).

to what is shown in 2-D models with externally imposed trenchward overriding plate motion and/or subducting plate motion, which generally show significant slab flattening and flat slab subduction (e.g. van Hunen *et al.* 2002; Liu & Currie 2016). The difference can be explained by the fact that in the buoyancy-driven model the subduction rate dramatically decreases during plateau subduction due to the smaller upper mantle slab negative buoyancy force, which causes the wedge suction force to drop and the slab to steepen. In the models with velocity boundary conditions, the subduction rate remains constant during plateau subduction, and the plateau is forced under the overriding plate at a faster rate than it would sink under buoyancy forces only, hence forcing plateau underplating.

4.2 Flat slab termination mechanism

Flat slab termination, as occurred for the Farallon slab in North America in the Eocene (Henderson *et al.* 1984; Liu *et al.* 2010) and the proto-Pacific slab in South China in the Jurassic (Li & Li 2007), could be ascribed to the ending or migration of ridge/plateau subduction (e.g. Henderson *et al.* 1984; Li & Li 2007), which changes the slab buoyancy, or to slab tearing (e.g. Antonijevic *et al.* 2015; Schepers *et al.* 2017) or slab window formation to allow for in-flow of subslab mantle into the mantle wedge region (e.g. Schellart *et al.* 2010; Király *et al.* 2020), thereby releasing both the underpressure in the mantle wedge and the overpressure in the subslab mantle. In the reference model and models BA50, SP60 and SP100, however, the flat slab disappears without such occurrences. Instead,

flat slab termination happens when the leading part of the overriding plate has been thickened considerably (from 60 km to max. ~ 110 – 120 km for the reference model). During the slab flattening phase and flat slab subduction phase, thickening is maximum above the central part of the flat slab segment and the distal flat slab hinge (Figs 5a–d, 7, 9a–b and 15a–b). The thickening forces this part of the slab downward, thereby increasing its dip angle (δ) near the distal hinge (Figs 15c–d). Overriding plate thickening also increases the dip angle of the overriding plate base (β) near the distal hinge (Figs 5b–e, 15b–c). A consequence of this and the slab steepening is that α increases rapidly after 135 Myr (Figs 4h and 15c). As the mantle wedge tip progressively widens, the vertical suction stress decreases in the mantle wedge while the effective suction force decreases more so due to the slab steepening (Fig. 6c). The vertical stresses in the ambient mantle can no longer sustain the flat slab, thereby ending the phase of flat slab subduction.

The termination of flat slab subduction is facilitated through small-scale upper mantle poloidal flow, as demonstrated in the reference model, which results from the straightening of the slab. The lower part of the upper mantle slab (between ~ 200 and 660 km) has an upper, gentle-dipping, segment (~ 30 – 40°) that is sinking in a \sim slab-dip parallel fashion and a lower, subvertical, segment that pushes mantle material \sim subhorizontally towards the overriding plate side, and then up and towards the subducting plate side (Figs 15c–d and 16d–e). This return flow cell in the mantle wedge facilitates the slab to straighten out and remove the flat slab segment at shallow levels. In the numerical model, the underpressure in the

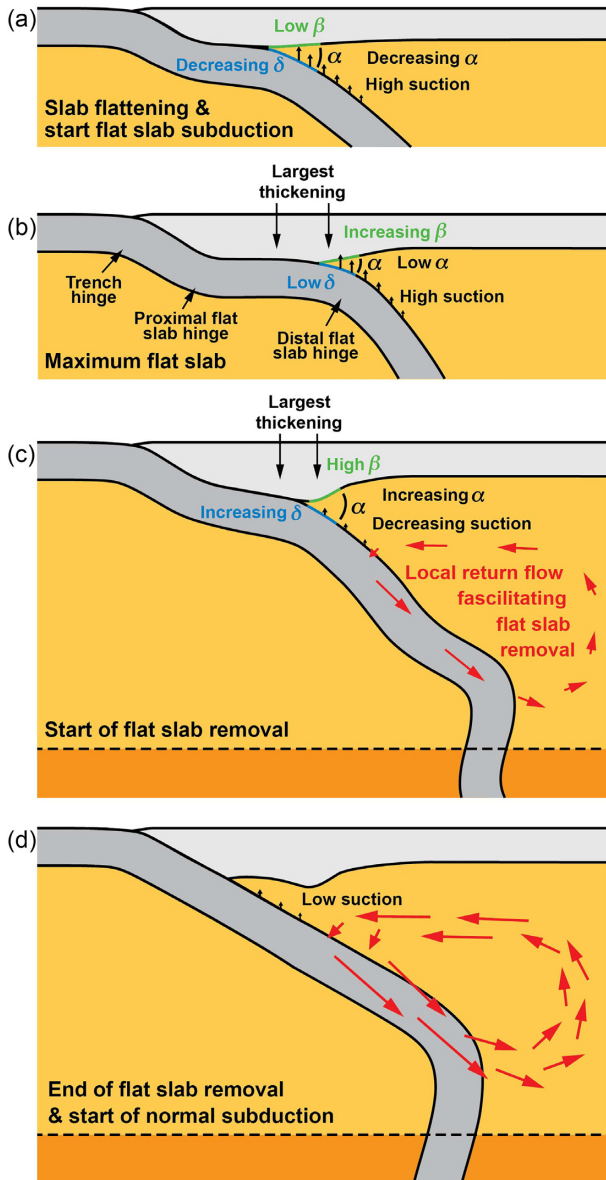


Figure 15. Schematic conceptual model of flat slab termination and geometric evolution of the mantle wedge. (a) Slab flattening and start of flat slab subduction during decreasing mantle wedge tip angle (α), low overriding plate basal slope (β), and decreasing slab top dip angle (δ). (b) Maximum flat slab during high wedge suction, an increasing β due to major overriding plate thickening above the flat slab and distal flat slab hinge, low δ and low α . (c) Start of flat slab removal during decreasing suction, high β , and increasing δ and α . (d) End phase of flat slab removal and start of normal subduction.

tip of the mantle wedge is thus not released through inflow from the subslab region through a slab tear or window, but through inflow from the lower part of the mantle wedge.

The cause for termination of flat slab subduction in western North America is unclear, but might be associated with the passing of a large oceanic plateau. Here an alternative model is proposed, or at least an additional contributing factor, in which lithospheric thickening at the Laramide orogen located near the distal flat slab hinge in the east forced mantle wedge tip opening. This would have reduced the wedge suction and would ultimately have resulted

in collapse of the flat slab and resumption of normal subduction, similar to the mechanism illustrated in Fig. 15.

4.3 Flat slab length

For most models the flat slab length is about 150–200 km. The lowest flat slab length of ~120 km was observed for model SP60 (Fig. 7a) and the highest flat slab length of ~250 km for model SP100-BA400 (Fig. 14). Such flat slab dimensions are sufficient to explain the ~150-, ~200- and ~250-km-long flat slab segments in Mexico, Central Peru and Central Chile, respectively (Figs 1i, k, l). They are, however, on the short side to explain all of the ~300-km-long flat slab segment in Northern Peru (Fig. 1j). Here, the extra 50–150 km of flat slab can be attributed to the extra lift of the Inca Plateau, a relatively buoyant plateau that has been proposed by Gutscher *et al.* (1999) to be the cause for flat slab subduction. The modelled flat slab lengths are likely too short to explain the entire flat slab that existed in North America during the Laramide orogeny. With a maximum trench-arc distance of ~1000 km (Coney & Reynolds 1977), and assuming a trench-proximal flat slab hinge distance of ~300 km and a flat slab edge-distal flat slab hinge distance of ~100 km (e.g. Fig. 1j), then the Laramide flat slab segment would have been ~600 km in trench-normal length. This is evidently much longer than the flat slab lengths modelled here (~150–250 km). The combination of strong trenchward motion of the overriding North American Plate, subduction of aseismic ridges/oceanic plateaus during flat slab subduction (e.g. Henderson *et al.* 1984; Liu *et al.* 2010; Liu & Currie 2016), and the wide slab setting and long subduction history (Schellart 2020) could be invoked to explain the extraordinary length of the flat slab segment.

Earlier geodynamic models of flat slab subduction show flat slab lengths that are generally somewhat higher than reported here, with maximum lengths of ~300 km (van Hunen *et al.* 2002; Rodríguez-González *et al.* 2012), ~350 km (van Hunen *et al.* 2004; Manea & Gurnis 2007; Gerya *et al.* 2009), ~400 km (Arcay *et al.* 2008), ~500 km (van Hunen *et al.* 2000) and ~700 km (Liu & Currie 2016). What all these earlier models have in common is that plate motion and/or trench motion were externally forced, rather than buoyancy-driven as in this work. A certain amount of external forcing can be justified (if quantified and properly scaled with respect to available buoyancy forces), in case the model represents a flat slab subduction segment that forms part of a larger subduction zone that includes segments without flat slab subduction, such that the flat-slab-free subduction segments provide an additional subduction drive to the flat slab subduction segment. However, in models with a 2-D spatial set-up this can evidently never be the case due to the implied infinite slab width with invariable geometry in the third dimension, which means an infinitely wide (trench-parallel) flat slab. A next step forward in simulating spatially confined flat slab subduction could thus be to test and study flat slab formation using buoyancy-driven models with a 3-D spatial set-up. A difficulty here could be that this would require major computational resources, considering that recent work has shown that, in a buoyancy-driven environment, flat slab development only occurs in the centre of very wide subduction zones after prolonged subduction into the deep lower mantle (Schellart 2020). This requires investigating the long-term evolution of subduction models in very large modelling domains.

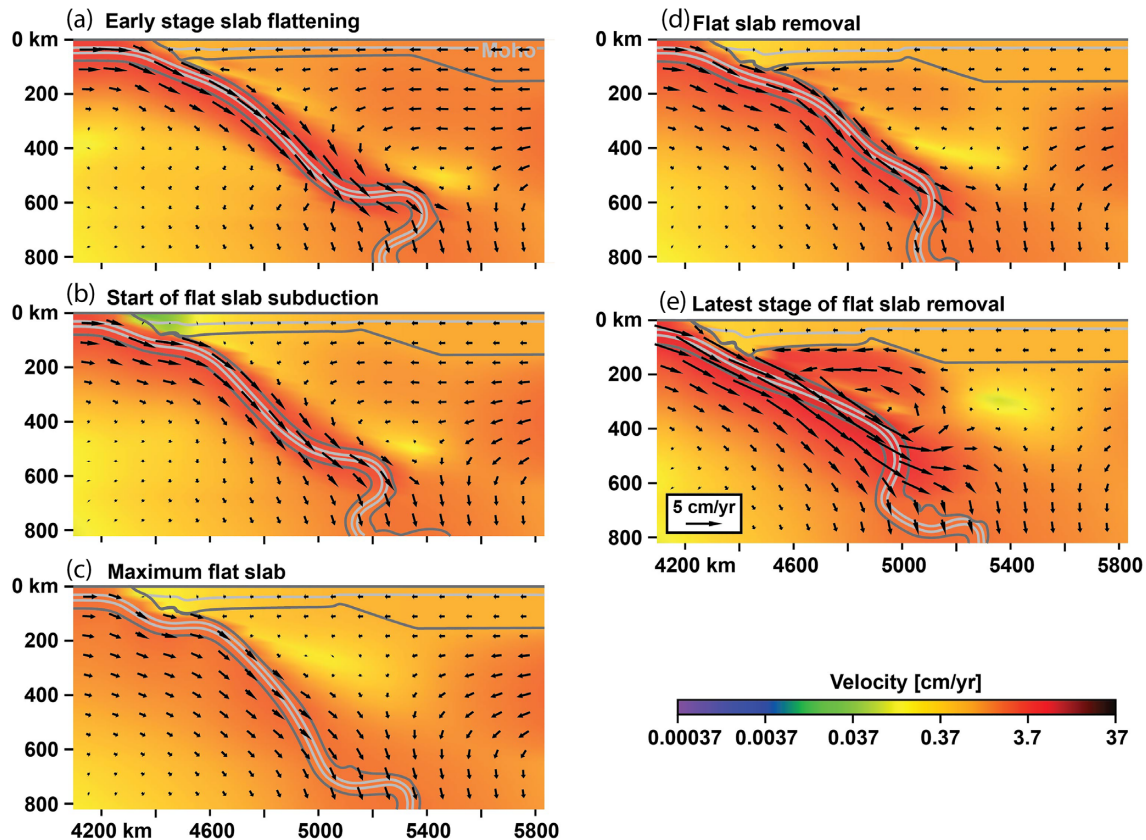


Figure 16. Numerical results of the reference model at high resolution (Reference.HighRes) showing the velocity field during slab flattening, flat slab subduction and flat slab removal. Dark grey lines show outlines of subducting plate, slab and overriding plate, while light grey lines show Moho in overriding plate and internal layering in subducting plate and slab.

4.4 Flat slab duration

Duration of the flat slab phase depends significantly on overriding plate backarc strength (Figs 7 and 8). A stronger overriding plate thickens more slowly and thereby sustains the flat slab for longer as the base of the overriding plate remains relatively flat for longer, thereby retarding the increase in overriding plate basal slope β . This is demonstrated with the reference model and models BA50, BA200 and BA400 (Fig. 8) in which the overriding plate backarc non-dimensional viscosity varies between 50 and 400. For BA400 the flat slab phase lasts at least 75 Myr, from ~ 116 Myr until the end of the model run at 191 Myr, which is much longer than for BA50 (6 Myr).

Those subduction segments in nature that have an active flat slab acquired their flat slab at ~ 8 Ma [Central Peru; Rosenbaum *et al.* (2005)], ~ 4 Ma [Southern Peru; Rosenbaum *et al.* (2005)], ~ 20 Ma [Central Chile; Kay & Abbruzzi (1996)] and 30–25 Ma [Mexico; Ferrari *et al.* (1999), Morán-Zenteno *et al.* (1999), Kim *et al.* (2010)]. Considering that these flat slab conditions might continue into the future for many millions of years, the flat slab durations of 8, 4, 20 and 25–30 Myr should be considered as a minimum. Nevertheless, such durations are of the same order of magnitude as observed for the reference model (18 Myr) and models SP60 (25 Myr), SP100 (8 Myr), BA50 (6 Myr) and SP100-B400 (≥ 51 Myr).

Several older phases of flat slab subduction along the South American subduction margin have been reported to last approximately 10–25 Myr (Horton 2018), which is again very comparable to the flat slab duration in a number of models presented here. The

Laramide flat slab subduction phase lasted ~ 30 Myr (Humphreys 2009), a duration which is comparable to that of model SP60 (25 Myr) and intermediate to what is observed for the reference model (~ 18 Myr) and BA400 (≥ 75 Myr). The flat slab subduction phase that has been proposed to explain the broad intracontinental Mesozoic orogen in South China lasted some 40 Myr, from the mid Triassic (~ 230 Ma) until the Early Jurassic (~ 190 Ma, Li & Li 2007). Such a duration is intermediate to what is observed for the reference model and model BA400.

4.5 Short-lived, long-lived and periodic flat slab subduction

From the model results presented in Figs 8, 9, 11 and 14 one can define three modes of flat slab subduction, the first two being short-lived, transient, flat slab subduction (e.g. Figs 8a and 9c) and long-lived flat slab subduction (e.g. Figs 8g, 11c and 14d). The third type is periodic flat slab subduction (e.g. Figs 8e and 9d). It is best observed for model BA200 showing periodic changes in δ_f with long periods of flat slab subduction followed by short periods where $\delta_f > 10^\circ$ (Fig. 8e). Model BA400 shows comparable behaviour with periodic changes in δ_f , but δ_f does not exceed 10° and so flat slab subduction is continuous (following our definition of flat slab subduction) (Fig. 8g). Periodic/episodic flat slab subduction and arc migration have recently been reported for the southern Central Andes (Horton 2018), which could tentatively be ascribed to the periodic folding at the 660 km discontinuity. The length scales of the periodic/episodic arc migration (~ 60 and ~ 80 km) can easily

be explained by the periodic dip angle changes (see also Schellart 2017), but the timescale of periodicity in nature ($\sim 50\text{--}60$ Myr) is larger than that observed in the models ($10\text{--}30$ Myr). The periodic subduction behaviour could also be possibly linked with the cyclic or episodic nature of continental and oceanic magmatic arcs (e.g. DeCelles *et al.* 2009; Ducea *et al.* 2015; Triantafyllou *et al.* 2020).

For all models, δ_s remains almost constant during flat slab subduction, for example ranging between 18.5° and 20° for model BA400 (Fig. 8g). During long-lived flat slab subduction δ_f changes periodically (periodicity of $\sim 10\text{--}30$ Myr) for all models, for example between -3° and 9° for model BA400, except for model LM10. The periodic change in δ_f and the periodic flat slab subduction result directly from the periodic slab folding at the 660 km discontinuity (Figs 3, 12 and A1). Indeed, the lack of periodic slab folding in model LM10 explains the absence in periodic slab dip angle changes and periodic velocities (Figs 11c–e).

For those models with periodic changes in δ_f , the local minima (i.e. times when the flat slab is most pronounced, white arrows in Figs 8e–h) generally correspond with low subducting plate and trench velocities, and thus low subduction rates. This results from the higher shear tractions, because the contact area between the subducting and overriding plates is highest at such times, as well as the lower slab pull transmitted to the subducting plate (Fig. 4i). The intervening local maxima in δ_f (i.e. times when the flat slab is absent or less pronounced, black arrows in Figs. 8e–h) generally correspond with high subducting plate velocities and higher trench velocities, and thus high subduction rates, because the contact area, and thus shear resistance, is lowest at these times and because the slab pull transmitted to the subducting plate is higher. Such periodic behaviour of subduction rates could possibly cause cyclic or episodic variations in productivity of continental and oceanic magmatic arcs.

5 CONCLUSIONS

Our buoyancy-driven numerical simulations of progressive subduction provide support for the conceptual model of flat slab formation in which lower mantle slab penetration and whole mantle subduction are required to produce a strong poloidal flow cell below the overriding plate. This flow cell drags the overriding plate trenchward, causing the upper mantle slab dip angle to decrease progressively over time, as the subduction zone hinge is actively being pushed back while the deeper portions of the slab in the upper mantle and lower mantle are not pushed backwards (Fig. 13). The low slab dip angle enhances mantle wedge suction, especially in the centre of a wide subduction zone (Dvorkin *et al.* 1993; Schellart 2020), promoting flat slab formation. The models indicate that, apart from mantle wedge suction supporting flat slabs, and to a lesser extent vertical compression at the base of the flat slab, slab folding at the 660 km discontinuity also plays an important role as the buckling slab periodically supports a relatively low slab dip in the shallow upper mantle through transmitting in-plane compressive stresses from the 660 km discontinuity upward. Such folding continues to play a role during flat slab subduction, producing periodic changes in the dip angle of the flat slab segment, which can lead to periodic flat slab subduction and periodic migration of arc magmatism.

The numerical models have shown that flat slab subduction can be reproduced in a buoyancy-driven environment without external forcing of plate motion, plate boundary motion or mantle flow. The models have also demonstrated that flat slab subduction can occur without plateau/ridge subduction and during slow-negligible trench

migration rates, in most models ranging between -0.5 cm yr^{-1} (advance) and 1.0 cm yr^{-1} (retreat). In fact, the models show that, in a 2-D buoyancy-driven environment, subduction of a plateau counters the formation of a flat slab, as it slows down subduction and causes a steepening of the shallow slab.

Finally, the models have shown that flat slab subduction disappears due to the local overriding plate shortening and thickening it produces, which forces mantle wedge opening and a reduction in effective mantle wedge suction, causing collapse of the flat slab (Fig. 15). As such, local slab tearing or passing of a buoyant aseismic ridge/plateau is not required to explain flat slab termination. Considering that overriding plate strength has a major control on the shortening rate and the periodic nature thereof, it has a strong control on the duration of flat slab subduction, which increases with increasing strength. As such, it is this parameter that also has a major control on the style of flat slab subduction, be it short-lived, transient, flat slab subduction for a weak backarc, periodic flat slab subduction for an intermediate-strength backarc and long-lived flat slab subduction for a strong backarc. Surprisingly, periodic flat slab subduction does not produce periodic overriding plate deformation. Rather, periodic overriding plate deformation is found to occur prior to flat slab subduction and is most pronounced with a weak backarc, as demonstrated with our geodynamic models (Fig. 8).

ACKNOWLEDGEMENTS

Discussions with Joao Duarte, Marc-Andre Gutscher and Filipe Rosas on subduction dynamics and flat slab subduction are greatly appreciated. We would like to thank the journal reviewers Gideon Rosenbaum and Dan Sandiford for providing constructive comments that have improved the contents of the paper. We would further like to thank Louis Moresi, Mirko Velic, Julian Giordani, John Mansour and Owen Kaluza for technical support with, and development of, the Underworld code. This work has been funded by a Vici Fellowship (016.VICI.170.110) from the Dutch National Science Foundation (NWO) awarded to WPS, and has been supported by computational resources from the National Computational Infrastructure in Australia through the National Computational Merit Allocation Scheme (project qk0), and computational resources from SURFsara, the Dutch national supercomputer facility, through project number 2019.055.

Author Contribution Statement: WPS conceived the study, developed and ran the numerical models and prepared the first draft of the manuscript. Both authors contributed towards analysing and interpreting the model results and towards editing of the paper.

DATA AVAILABILITY

All data, results and methods that are necessary to understand, evaluate, replicate, and build upon the reported research are presented in the manuscript. The *Underworld* code that was used to generate the numerical models is an open-source code and is available at <https://www.underworldcode.org>. Source data underlying this article will be shared on reasonable request to the corresponding author.

REFERENCES

- Antonijeveć, S.K., Wagner, L.S., Kumar, A., Beck, S.L., Long, M.D., Zandt, G., Tavera, H. & Condori, C., 2015. The role of ridges in the formation and longevity of flat slabs, *Nature*, **524**, 212–215.

- Arcay, D., Lallemand, S. & Doin, M.-P., 2008. Back-arc strain in subduction zones: statistical observations versus numerical modeling, *Geochem. Geophys. Geosyst.*, **9**, Q05015, doi:10.1029/2007GC001875.
- Arredondo, K.M. & Billen, M.I., 2016. The effects of phase transitions and compositional layering in two-dimensional kinematic models of subduction, *J. Geodyn.*, **100**, 159–174.
- Barazangi, M. & Isacks, B.L., 1976. Spatial distribution of earthquakes and subduction of the Nazca plate beneath South America, *Geology*, **4**, 686–692.
- Běhouňková, M. & Čížková, H., 2008. Long-wavelength character of subducted slabs in the lower mantle, *Earth planet. Sci. Lett.*, **275**, 43–53.
- Bina, C.R., Čížková, H. & Chen, P.-F., 2020. Evolution of subduction dip angles and seismic stress patterns during arc-continent collision: modeling Mindoro Island, *Earth planet. Sci. Lett.*, **533**, 116054, doi:10.1016/j.epsl.2019.116054.
- Bird, P., 1984. Laramide crustal thickening event in the Rocky Mountain foreland and great plains, *Tectonics*, **3**, 741–758.
- Burchfiel, B.C. & Davis, G.A., 1975. Nature and controls of cordilleran orogenesis, Western United States: extensions of an earlier synthesis, *Am. J. Sci.*, **275-A**, 363–396.
- Christensen, U.R., 1996. The influence of trench migration on slab penetration into the lower mantle, *Earth planet. Sci. Lett.*, **140**, 27–39.
- Čížková, H. & Bina, C.R., 2013. Effects of mantle and subduction-interface rheologies on slab stagnation and trench rollback, *Earth planet. Sci. Lett.*, **379**, 95–103.
- Coira, B., Davidson, J., Mpodozis, C. & Ramos, V., 1982. Tectonic and magmatic evolution of the Andes of northern Argentina and Chile, *Earth Sci. Rev.*, **18**, 303–332.
- Collins, W.J., 2003. Slab pull, mantle convection, and Pangaean assembly and dispersal, *Earth planet. Sci. Lett.*, **205**, 225–237.
- Coney, P.J. & Reynolds, S.J., 1977. Cordilleran Benioff zones, *Nature*, **270**, 403–406.
- Currie, C.A. & Hyndman, R.D., 2006. The thermal structure of subduction zone back arcs, *J. geophys. Res.*, **111**, B08404, doi:10.1029/2005JB004024.
- Davies, G.F., 1999. *Dynamic Earth: Plates, Plumes and Mantle Convection*, Cambridge Univ. Press, pp. 460.
- Davies, G.F. & Richards, M.A., 1992. Mantle convection, *J. Geol.*, **100**, 151–206.
- DeCelles, P.G., Ducea, M.N., Kapp, P. & Zandt, G., 2009. Cyclicity in cordilleran orogenic systems, *Nat. Geosci.*, **2**, 251–257.
- de Wijs, G.A., Kresse, G., Vocablo, L., Dobson, D., Alfè, D., Gillan, M.J. & Price, G.D., 1998. The viscosity of liquid iron at the physical conditions of the Earth's core, *Nature*, **392**, 805–807.
- Dickinson, W.R. & Snyder, W.S., 1978. Plate tectonics of the Laramide orogeny, *Geol. Soc. Am. Mem.*, **151**, 355–366.
- Domeier, M. & Torsvik, T.H., 2014. Plate tectonics in the late Paleozoic, *Geosci. Front.*, **5**, 303–350.
- Ducea, M.N., Saleeby, J.B. & Bergantz, G., 2015. The architecture, chemistry, and evolution of continental magmatic arcs, *Ann. Rev. Earth planet. Sci.*, **43**, 299–331.
- Dvorkin, J., Nur, A., Mavko, G. & Ben-Avraham, Z., 1993. Narrow subducting slabs and the origin of backarc basins, *Tectonophysics*, **227**, 63–79.
- Espurt, N., Funicello, F., Martinod, J., Guillaume, B., Regard, V., Faccenna, C. & Brusset, S., 2008. Flat subduction dynamics and deformation of the South American plate: insights from analog modeling, *Tectonics*, **27**, TC3011, doi:10.1029/2007TC002175.
- Ferrari, L., López-Martínez, M., Aguirre-Díaz, G. & Carrasco-Núñez, G., 1999. Space-time patterns of Cenozoic arc volcanism in central Mexico: from the Sierra Madre Occidental to the Mexican Volcanic Belt, *Geology*, **27**, 303–306.
- Flórez-Rodríguez, A.G., Schellart, W.P. & Strak, V., 2019. Impact of aseismic ridges on subduction systems: insights from analog modeling, *J. geophys. Res.*, **124**, 5951–5969.
- Forsyth, D.W. & Uyeda, S., 1975. On the relative importance of the driving forces of plate motion, *Geophys. J. R. astr. Soc.*, **43**, 163–200.
- Garel, F., Goes, S., Davies, D.R., Davies, J.H., Kramer, S.C. & Wilson, C.R., 2014. Interaction of subducted slabs with the mantle transition-zone: a regime diagram from 2-D thermo-mechanical models with a mobile trench and an overriding plate, *Geochem. Geophys. Geosyst.*, **15**, 1739–1765.
- Gerya, T.V., Fossati, D., Cantieni, C. & Seward, D., 2009. Dynamic effects of aseismic ridge subduction: numerical modelling, *Eur. J. Mineral.*, **21**, 649–661.
- Griffiths, R.W., Hackney, R.I. & van der Hilst, R.D., 1995. A laboratory investigation of effects of trench migration on the descent of subducted slabs, *Earth planet. Sci. Lett.*, **133**, 1–17.
- Gudmundsson, O. & Sambridge, M.J., 1998. A regionalized upper mantle (RUM) seismic model, *J. geophys. Res.*, **103**, 7121–7136.
- Guillou-Frottier, L., Buttles, J. & Olson, P., 1995. Laboratory experiments on the structure of subducted lithosphere, *Earth planet. Sci. Lett.*, **133**, 19–34.
- Gutscher, M.A., Olivet, J.L., Aslanian, D., Eissen, J.P. & Maury, R., 1999. The “lost Inca Plateau”: cause of flat subduction beneath Peru? *Earth planet. Sci. Lett.*, **171**, 335–341.
- Gutscher, M.A., Spakman, W., Bijwaard, H. & Engdahl, E.R., 2000. Geodynamics of flat subduction: seismicity and tomographic constraints from the Andean margin, *Tectonics*, **19**, 814–833.
- Hager, B.H., 1984. Subducted slabs and the geoid: constraints on mantle rheology and flow, *J. geophys. Res.*, **89**, 6003–6015.
- Harig, C., Zhong, S. & Simons, F.J., 2010. Constraints on upper mantle viscosity from the flow-induced pressure gradient across the Australian continental keel, *Geochem. Geophys. Geosyst.*, **11**, Q06004, doi:10.1029/2010GC003038.
- Hayes, G.P., Wald, D.J. & Johnson, R.L., 2012. Slab1.0: a three-dimensional model of global subduction zone geometries, *J. geophys. Res.*, **117**, B01302, doi:10.1029/2011JB008524.
- Henderson, L.J., Gordon, R.G. & Engebretson, D.C., 1984. Mesozoic aseismic ridges on the Farallon plate and southward migration of shallow subduction during the Laramide orogeny, *Tectonics*, **3**, 121–132.
- Horton, B.K., 2018. Tectonic regimes of the central and southern Andes: responses to variations in plate coupling during subduction, *Tectonics*, **37**, 402–429.
- Hu, J., Liu, L., Hermsillo, A. & Zhou, Q., 2016. Simulation of late Cenozoic South American flat-slab subduction using geodynamic models with data assimilation, *Earth planet. Sci. Lett.*, **438**, 1–13.
- Humphreys, E., 2009. Relation of flat subduction to magmatism and deformation in the western United States, *Geol. Soc. Am. Mem.*, **204**, 85–98.
- James, T.S., Gowan, E.J., Wada, I. & Wang, K., 2009. Viscosity of the asthenosphere from glacial isostatic adjustment and subduction dynamics at the northern Cascadia subduction zone, British Columbia, Canada, *J. geophys. Res.*, **114**, B04405, doi:10.1029/2008JB006077.
- Jarrard, R.D., 1986. Relations among subduction parameters, *Rev. Geophys.*, **24**, 217–284.
- Kaufmann, G. & Lambeck, K., 2000. Mantle dynamics, postglacial rebound and the radial viscosity profile, *Phys. Earth planet. Inter.*, **121**, 301–324.
- Kay, S.M. & Abbruzzi, J.M., 1996. Magmatic evidence for Neogene lithospheric evolution of the central Andean “flat-slab” between 30 S and 32 S, *Tectonophysics*, **259**, 15–28.
- Kim, Y., Clayton, R.W. & Jackson, J.M., 2010. Geometry and seismic properties of the subducting Cocos plate in central Mexico, *J. geophys. Res.*, **115**, B06310, doi:10.1029/2009JB006942.
- Királya, Á. et al., 2020. The effect of slab gaps on subduction dynamics and mantle upwelling, *Tectonophysics*, **785**, 228458, doi:10.1016/j.tecto.2020.228458.
- Lallemand, S., Heuret, A. & Boutelier, D., 2005. On the relationship between slab dip, back-arc stress, upper plate absolute motion, and crustal nature in subduction zones, *Geochem. Geophys. Geosyst.*, **6**, Q09006, doi:10.1029/2005GC000917.
- Lee, C. & King, S.D., 2011. Dynamic buckling of subducting slabs reconciles geological and geophysical observations, *Earth planet. Sci. Lett.*, **312**, 360–370.
- Liu, L., Gurnis, M., Seton, M., Saleeby, J., Muller, R.D. & Jackson, J.M., 2010. The role of oceanic plateau subduction in the Laramide orogeny, *Nat. Geosci.*, **3**, 353–357.

- Liu, S. & Currie, C.A., 2016. Farallon plate dynamics prior to the Laramide orogeny: numerical models of flat subduction, *Tectonophysics*, **666**, 33–47.
- Li, Z.-X. & Li, X.-H., 2007. Formation of the 1300-km-wide intracontinental orogen and postorogenic magmatic province in Mesozoic South China: a flat-slab subduction model, *Geology*, **35**, 179–182.
- Manea, V. & Gurnis, M., 2007. Subduction zone evolution and low viscosity wedges and channels, *Earth planet. Sci. Lett.*, **264**, 22–45.
- Manea, V.C., Manea, M., Ferrari, L., Orozco-Esquivel, T., Valenzuela, R.W., Husker, A. & Kostoglodov, V., 2017. A review of the geodynamic evolution of flat slab subduction in Mexico, Peru, and Chile, *Tectonophysics*, **695**, 27–52.
- Manea, V.C., Pérez-Gussinyé, M. & Manea, M., 2012. Chilean flat slab subduction controlled by overriding plate thickness and trench rollback, *Geology*, **40**, 35–38.
- Marot, M., Monfret, T., Gerbault, M., Nolet, G., Ranalli, G. & Pardo, M., 2014. Flat versus normal subduction zones: a comparison based on 3-D regional traveltimes tomography and petrological modelling of central Chile and western Argentina (29–35S), *Geophys. J. Int.*, **199**, 1633–1654.
- Morán-Zenteno, D.J. *et al.*, 1999. Tertiary arc-magmatism of the Sierra Madre del Sur, Mexico, and its transition to the volcanic activity of the Trans-Mexican Volcanic Belt, *J. S. A. Earth Sci.*, **12**, 513–535.
- Moresi, L., Dufour, F. & Mühlhaus, H.-B., 2003. A Lagrangian integration point finite element method for large deformation modeling of viscoelastic geomaterials, *J. Comput. Phys.*, **184**, 476–497.
- Moresi, L., Quenette, S., Lemiale, V., Mériaux, C., Appelbe, B. & Mühlhaus, H.-B., 2007. Computational approaches to studying non-linear dynamics of the crust and mantle, *Phys. Earth planet. Inter.*, **163**, 69–82.
- Nakajima, J. & Hasegawa, A., 2007. Subduction of the Philippine Sea plate beneath southwestern Japan: slab geometry and its relationship to arc magmatism, *J. geophys. Res.*, **112**, B08306, doi:10.1029/2006JB004770.
- Ohta, Y., Freymueller, J.T., Hreinsdóttir, S. & Suito, H., 2006. A large slow slip event and the depth of the seismogenic zone in the south central Alaska subduction zone, *Earth planet. Sci. Lett.*, **247**, 108–116.
- Olbertz, D., Wortel, M.J.R. & Hansen, U., 1997. Trench migration and subduction zone geometry, *Geophys. Res. Lett.*, **24**, 221–224.
- Palmer, A. & Smylie, D.E., 2005. VLBI observations of free core nutations and viscosity at the top of the core, *Phys. Earth planet. Inter.*, **148**, 285–301.
- Peltier, W.R., 2004. Global glacial isostasy and the surface of the ice-age Earth: the ICE-5G (VM2) model and grace, *Ann. Rev. Earth planet. Sci.*, **32**, 111–149.
- Pérez-Campos, X. *et al.*, 2008. Horizontal subduction and truncation of the Cocos Plate beneath central Mexico, *Geophys. Res. Lett.*, **35**, L18303, doi:10.1029/2008GL035127.
- Phillips, K. & Clayton, R.W., 2014. Structure of the subduction transition region from seismic array data in southern Peru, *Geophys. J. Int.*, **196**, 1889–1905.
- Pilger, R.H., 1981. Plate reconstructions, aseismic ridges, and low-angle subduction beneath the Andes, *Bull. geol. Soc. Am.*, **92**, 448–456.
- Ramos, V.A. & Folguera, A. (2009), Andean flat-slab subduction through time, in *Ancient Orogens and Modern Analogues*, pp. 31–54, eds Murphy, J.B., Keppie, J.D. & Hynes, A.J., The Geological Society of London, doi:10.1144/SP327.3.
- Ribe, N.M., 2010. Bending mechanics and mode selection in free subduction: a thin-sheet analysis, *Geophys. J. Int.*, **180**, 559–576.
- Ribe, N.M., Stutzmann, E., Ren, Y. & van der Hilst, R., 2007. Buckling instabilities of subducted lithosphere beneath the transition zone, *Earth planet. Sci. Lett.*, **254**, 173–179.
- Rodríguez-González, J., Negrodo, A.M. & Billen, M.I., 2012. The role of the overriding plate thermal state on slab dip variability and on the occurrence of flat subduction, *Geochem. Geophys. Geosyst.*, **13**, Q01002, doi:10.1029/2011GC003859.
- Rosenbaum, G., Giles, D., Saxon, M., Betts, P.G., Weinberg, R.F. & Duboz, C., 2005. Subduction of the Nazca Ridge and the Inca Plateau: insights into the formation of ore deposits in Peru, *Earth planet. Sci. Lett.*, **239**, 18–32.
- Rutter, M.D., Secco, R.A., Uchida, T., Hongjian, L., Wang, Y., Rivers, M.L. & Sutton, S.R., 2002. Towards evaluating the viscosity of the Earth's outer core: an experimental high pressure study of liquid Fe-S (8.5 wt.% S), *Geophys. Res. Lett.*, **29**, 1217, doi:10.1029/2001GL014392.
- Sandiford, D., Moresi, L.M., Sandiford, M., Farrington, R. & Yang, T., 2020. The fingerprints of flexure in slab seismicity, *Tectonics*, **39**, e2019TC005894, doi:10.1029/2019TC005894.
- Schellart, W.P., 2005. Influence of the subducting plate velocity on the geometry of the slab and migration of the subduction hinge, *Earth planet. Sci. Lett.*, **231**, 197–219.
- Schellart, W.P., 2008a. Overriding plate shortening and extension above subduction zones: a parametric study to explain formation of the Andes mountains, *Bull. geol. Soc. Am.*, **120**, 1441–1454.
- Schellart, W.P., 2008b. Kinematics and flow patterns in deep mantle and upper mantle subduction models: influence of the mantle depth and slab to mantle viscosity ratio, *Geochem. Geophys. Geosyst.*, **9**, Q03014, doi:10.1029/2007GC001656.
- Schellart, W.P., 2017. Andean mountain building and magmatic arc migration driven by subduction-induced whole mantle flow, *Nat. Commun.*, **8**, doi:10.1038/s41467-017-01847-z.
- Schellart, W.P., 2020. Control of subduction zone age and size on flat slab subduction, *Front. Earth Sci.*, **8**, 26, doi:10.3389/feart.2020.00026.
- Schellart, W.P., Freeman, J., Stegman, D.R., Moresi, L. & May, D., 2007. Evolution and diversity of subduction zones controlled by slab width, *Nature*, **446**, 308–311.
- Schellart, W.P. & Moresi, L., 2013. A new driving mechanism for backarc extension and backarc shortening through slab sinking induced toroidal and poloidal mantle flow: results from dynamic subduction models with an overriding plate, *J. geophys. Res.*, **118**, 3221–3248.
- Schellart, W.P., Stegman, D.R., Farrington, R.J., Freeman, J. & Moresi, L., 2010. Cenozoic tectonics of western North America controlled by evolving width of Farallon slab, *Science*, **329**, 316–319, doi:10.1126/science.1190366.
- Schellart, W.P. & Strak, V., 2016. A review of analogue modelling of geodynamic processes: approaches, scaling, materials and quantification, with an application to subduction experiments, *J. Geodyn.*, **100**, 7–32.
- Schepers, G., van Hinsbergen, D.J.J., Spakman, W., Kesters, M.E., Boschman, L.M. & McQuarrie, N., 2017. South-American plate advance and forced Andean trench retreat as drivers for transient flat subduction episodes, *Nat. Commun.*, **8**, 15249, doi:10.1038/ncomms15249.
- Shemenda, A., 1993. Subduction of the lithosphere and back arc dynamics: insights from physical modeling, *J. geophys. Res.*, **98**, 16 167–16 185.
- Skinner, S.M. & Clayton, R.W., 2011. An evaluation of proposed mechanisms of slab flattening in Central Mexico, *Pure appl. Geophys.*, **168**, 1461–1474.
- Skinner, S.M. & Clayton, R.W., 2013. The lack of correlation between flat slabs and bathymetric impactors in South America, *Earth planet. Sci. Lett.*, **371–372**, 1–5.
- Stegman, D.R., Farrington, R., Capitanio, F.A. & Schellart, W.P., 2010. A regime diagram for subduction styles from 3-D numerical models of free subduction, *Tectonophysics*, **483**, 29–45.
- Stegman, D.R., Freeman, J., Schellart, W.P., Moresi, L. & May, D., 2006. Influence of trench width on subduction hinge retreat rates in 3-D models of slab rollback, *Geochem. Geophys. Geosyst.*, **7**, Q03012, doi:10.1029/2005GC001056.
- Strak, V. & Schellart, W.P., 2021. Thermo-mechanical numerical modeling of the South American subduction zone: a multi-parametric investigation, *J. geophys. Res.*, **126**, doi:10.1029/2020JB021527.
- Tovish, A., Schubert, G. & Luyendyk, B.P., 1978. Mantle flow pressure and the angle of subduction: non-Newtonian corner flows, *J. geophys. Res.*, **83**, 5892–5898.
- Triantafyllou, A. *et al.*, 2020. Episodic magmatism during the growth of a Neoproterozoic oceanic arc (Anti-Atlas, Morocco), *Precambrian Res.*, **339**, 105610, doi:10.1016/j.precamres.2020.105610.
- van Hunen, J., van den Berg, A.P. & Vlaar, N.J., 2000. A thermo-mechanical model of horizontal subduction below an overriding plate, *Earth planet. Sci. Lett.*, **182**, 157–169.

- van Hunen, J., Van Den Berg, A.P. & Vlaar, N.J., 2002. On the role of subducting oceanic plateaus in the development of shallow flat subduction, *Tectonophysics*, **352**, 317–333.
- van Hunen, J., van den Berg, A.P. & Vlaar, N.J., 2004. Various mechanisms to induce present-day shallow flat subduction and implications for the younger Earth: a numerical parameter study, *Phys. Earth planet. Inter.*, **146**, 179–194.
- Yamaoka, K., Fukao, Y. & Kumazawa, M., 1986. Spherical shell tectonics: effects of sphericity and inextensibility on the geometry of the descending lithosphere, *Rev. Geophys.*, **24**, 27–53.
- Yang, T., Moresi, L., Gurnis, M., Liu, S., Sandiford, D., Williams, S. & Capitanio, F.A., 2019. Contrasted East Asia and South America tectonics driven by deep mantle flow, *Earth planet. Sci. Lett.*, **517**, 106–116.
- Zhong, S. & Gurnis, M., 1995. Mantle convection with plates and mobile, faulted plate margins, *Science*, **267**, 838–843.

APPENDIX A: RESOLUTION TESTS

The reference model has been run at three different resolutions to test its influence on the evolution of the subduction system, the kinematics of subduction and on the development of flat slab subduction. The resolutions that have been used are 512 by 192, 1024 by 512 and 2048 by 1024 elements. The models generally show a

very comparable evolution, in which the evolving slab geometry is close to identical in the three models. Indeed, during flat slab subduction the flat slab segment, the remaining upper mantle slab segment and the folded slab pile in the lower mantle are comparable in shape and size (Fig. A1). The evolution of the velocities, such as v_{SP} , v_T and v_S , is comparable as well, showing comparable velocity magnitudes, strongly periodic behaviour for v_{SP} and v_S , and less-developed periodic behaviour for v_T , which shows an overall decreasing trend towards negligible velocities during flat slab subduction (Fig. A2). The subduction partitioning v_{SP}/v_S is comparable as well, with a general increase in value with increasing time towards 1 at the end of each model run, and periodic behaviour superimposed on this long-term trend (Fig. A2d). The evolution of δ_f is very comparable as well, giving an overall decrease with progressive time with a periodic variation superimposed on this long-term trend, and a period of flat slab subduction in a late stage with a flat slab subduction angle close to 0° . From the curves and data plotted in Fig. A2 it is further clear that all velocities increase with increasing resolution, and that those curves and data for the standard and high-resolution models show considerable overlap, while those for the low-resolution model are somewhat more stretched along the time axis.

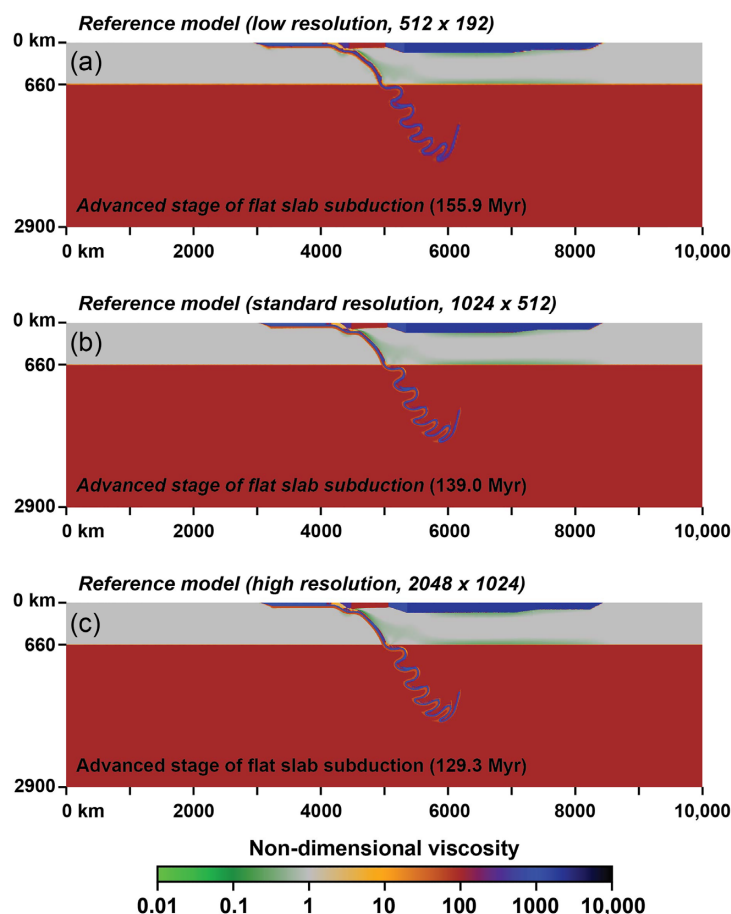


Figure A1. Results of resolutions tests for the reference model with three different spatial resolutions, showing model cross sections with the non-dimensional viscosity field, and with it the geometry of the slab, subducting plate and overriding plate. (a) Model Reference.LowRes with 512 (horizontal) by 192 (vertical) elements. (b) Reference model with the standard resolution (1024 by 512 elements). (c) Model Reference.HighRes with 2048 by 1024 elements. Note that the geometries in the models are nearly identical.

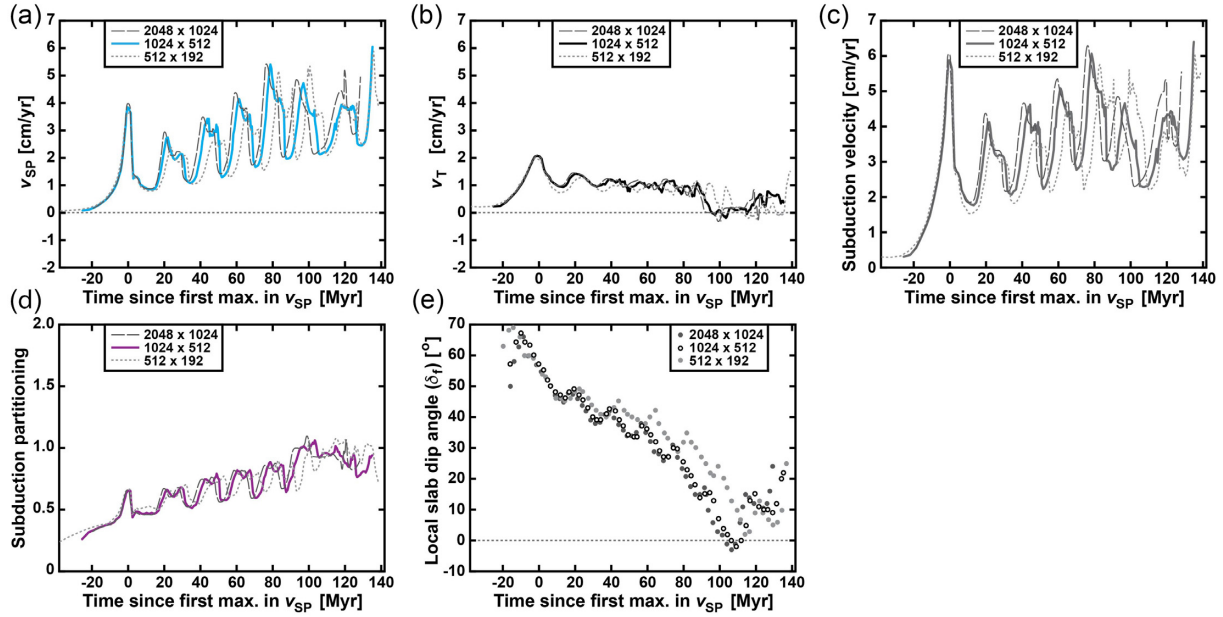


Figure A2. Results of resolution tests for the reference model with three different spatial resolutions (512×192 , 1024×512 , and 2048×1024 elements), showing the temporal evolution of the subduction zone kinematics and the local slab dip angle (δ_f). (a) Subducting plate velocity (v_{SP} , trenchward is positive). (b) Trench velocity (v_T , retreat is positive). (c) Subduction velocity ($v_S = v_T + v_{SP}$). (d) Subduction partitioning ratio (v_{SP}/v_S). (e) δ_f . Note that the results have been centred on the time of occurrence of the first maximum in v_{SP} , which occurs during the upper mantle subduction phase.